Anode partial flooding modelling of proton exchange membrane fuel cells

Xing, Lei; Du, Shangfeng; Chen, Rui; Mamlouk, Mohamed; Scott, Keith

DOI:
10.1016/j.energy.2015.12.048

Document Version
Peer reviewed version

Citation for published version (Harvard):
Xing, L, Du, S, Chen, R, Mamlouk, M & Scott, K 2016, 'Anode partial flooding modelling of proton exchange membrane fuel cells: model development and validation', Energy, vol. 96, pp. 80-95. https://doi.org/10.1016/j.energy.2015.12.048

Anode partial flooding modelling of Proton Exchange Membrane Fuel Cells: Model development and validation

Lei Xing[a,b,*], Shangfeng Du[b], Rui Chen[c], Mohamed Mamlouk[d] and Keith Scott[d]

a. Institute of Green Chemistry and Chemical Technology, Jiangsu University, Zhenjiang, 212013, China

b. School of Chemical Engineering, University of Birmingham, Edgbaston, Birmingham, B15 2TT, United Kingdom

c. School of Aeronautical and Automotive Engineering, Loughborough University, Leicestershire, LE11 3TU, United Kingdom

d. School of Chemical Engineering and Advanced Materials, Merz Court, Newcastle University, Newcastle upon Tyne, NE1 7RU, United Kingdom

Highlights

- A fully coupled 2D, along-the-channel, two-phase flow, non-isothermal, CFD model is developed.
- Temperature rise due to electrochemical reactions, ohmic resistance and water phase-transfer is analyzed.
- Mathematical expressions of liquid water saturation against current density at anode and cathode are regressed.
- Relationship between the liquid water saturation at anode and cathode is built.

Corresponding author:

School of Chemical Engineering, University of Birmingham, Edgbaston, Birmingham, B15 2TT, United Kingdom
Tel.: +44 (0)121 414 5081
Fax: +44 (0)121 414 5081
Email: xinglei1314@gmail.com; l.xing@bham.ac.uk

Shangfeng Du (S.Du@bham.ac.uk)
Rui Chen (r.chen@lboro.ac.uk)
Mohamed Mamlouk (m.mamlouk@ncl.ac.uk)
Keith Scott (k.scott@ncl.ac.uk)

Abstract

A two-dimensional along-the-channel computational fluid dynamic (CFD) model, coupled with a two-phase flow model of liquid water and gas transport for a proton exchange membrane (PEM) fuel cell is described. The model considers non-isothermal operation and thus the non-uniform temperature distribution in the cell structure. Water phase-transfer between the vapour, liquid water and dissolved phase is modelled with the combinational transport mechanism through the membrane. Liquid water saturation is simulated inside the electrodes and channels at both the anode and cathode sides. Three types of models are compared for the hydrogen oxidation reaction (HOR) and oxygen reduction reaction (ORR) in catalyst layers, including Butler-Volmer (B-V), liquid water saturation corrected B-V and agglomerate mechanisms. Temperature changes in membrane electrode assembly (MEA) and channels due to electrochemical reaction, ohmic resistance and water phase-transfer are analysed as a function of current density. Nonlinear relations of liquid water saturations with respect to current densities at both the anode and cathode are regressed. At low and high current densities, liquid water saturation in the anode linearly increases as a consequence of the linear increase of liquid water saturation in the cathode. In contrast, exponential relation is found to be more accurate at medium current densities.

Key works: PEMFC; liquid water; anode flooding; agglomerate model; non-isothermal; CFD

1. Introduction

Benefiting from high energy efficiency and low emission, proton exchange membrane fuel cells (PEMFCs), play an important role in transiting a carbon intensive economy to sustainable low carbon future [1-4]. In addition, the features of PEMFCs endow a flexibility and scalability for use with batteries and combined heat and power (CHP) system for hybrid automotive and residential use [5-7], as well as energy conversion between winds to electricity [8]. Among the PEMFC family, the medium and low temperature PEMFCs are considered as promising candidates as portable and automotive power sources. However, they can experience certain operating difficulties associated with water transport and flooding during their operation, especially at a high current density [9-11].

Three phases of water co-exist in PEMFCs: as vapor and liquid in porous electrodes and channels, and as a dissolved phase absorbed by membrane and ionomer (membrane and ionomer water uptake). Among three phases, dissolved water can migrate between both electrodes through the membrane under the driving forces of electro-osmotic drag (EOD), back diffusion and hydraulic permeation [12-14]. Liquid water can be generated in terms of water vapor condensation and membrane/ionomer desorption when over-saturated. Simultaneously, liquid water is removed from the MEA (membrane electrode assembly) generally by reactant gases flowing along the channels. If water generation rate is faster than the removal rate, excess water will accumulate in the electrodes and flow channels, leading to a water flooding inside the cell. This flooding can reduce the effective porosity in the porous media and increase the pressure drop along the channel, inhibiting the gas transport to the active sites in catalyst layers (CLs), finally resulting in a decline in the cell performance [15-17]. Water flooding is typically observed at the cathode side due to the fact that water is produced inside the cathode catalyst layers (CCLs) by the oxygen reduction reaction (ORR).

There have been numerous studies of water flooding at the cathode but less consideration of water transport related to the anode. However, hydrogen consumption at the anode could also results in the humidified anode reactant gas becoming supersaturated with water vapor, which can result in transfer to liquid water after condensation. Liquid water movement in hydrophilic and hydrophobic anode gas channel, as well as the effect of hydrogen inlet velocity, operating temperature and channel walls wettability, was numerically studied by Ferreira et al. [18]. Experimental studies have detected liquid water in the anode and that more liquid water was observed at a high anode relative humidity [19, 20]. An in-situ detection scheme of anode flooding, developed by O'Rourke et al. [21], showed that anode flooding could be detected prior to a rapid cell voltage decline, which was considered as an early warning of cathode catalyst damage. As reported by Anderson et al. [22], anode water removal (AWR) could be used as a diagnostic tool to assess cathode water flooding in PEM fuel cells.

Catalyst layers are complex structures and are a difficult to describe and be fully understood in PEMFCs; not only due to their highly compact structure and complex composition but also because of the coupled electrochemical reactions and transport processes occurred. CLs in PEMFCs facilitate electrochemical reactions and produce water at the cathode. To describe the current density produced on each electrode in fuel cell operation, considering the water generated which can partially cover the platinum catalyst surface, (1-s) corrected B-V equation (s is the liquid water saturation, defining as the volume fraction of void space occupied by liquid water) is usually required instead of the traditional B-V equation [23-25]. The electrochemical activity may be further represented using an agglomerate mode, taking into account the increase in ionomer film thickness surrounding the agglomerate due to ionomer swelling. Furthermore, by considering gas transport resistance and the reduction of porosity

due to liquid water occupation, the agglomerate model can also provide a superior representation of the porous CLs in comparison with other models [26, 27].

In fuel cell operation, temperature plays a significant role in achieving a high power performance. A variety of parameters, e.g. electrochemical reaction kinetics, mole fractions in gas mixture, electrolyte conductivity, rate of mass transfer, as well as liquid water saturation, are closely correlated with temperature during fuel cell operation. Within PEMFCs, the temperature distribution across the MEAs and along the flow channels can be either estimated by mathematical modelling technique or detected by experimental measurements [28-31]. Ju et al. [28] developed a three dimensional (3D), single-phase, non-isothermal model through a parametric study for GDL thermal conductivity, gas relative humidity and operating cell voltage. Wang et al. [29] measured the temperature profile within a single PEMFC with the aid of infrared thermal imaging (ITI) and found that the downstream temperature is higher than the upstream, and there was an obvious high temperature section in the outlet of oxygen. Temperature measurement were conducted by Zhang et al. [30] and Lin et al. [31] from which they found a correlation between local temperature rise and local current density, and a temperature rise at backsides of both the anode and cathode flow field plates.

However, up to now, it is still a challenge to fully couple most aspects mentioned above in modelling for a highly accurate evaluation of water flooding in a single PEMFC or stack. In this paper, we fully couple seven sub-models and apply them on a two dimensional (2D), along-the-channel (ATC) geometry for a single PEMFC: (1) agglomerate models for gas transport resistance in CLs, (2) two-phase flow models for liquid water saturation, (3) combinational diffusion models for dissolved water transport through the membrane, (4) non-isothermal models for heat transport in MEA and channels, (5) computational fluid dynamic (CFD) models for gas transport along the channels, (6)

multicomponent diffusion of reactant gases in gas mixture, and (7) ionomer swelling due to non-uniform distribution of water content. The effect of liquid water on the current density are compared based on three mechanisms, including traditional B-V, (1-s) corrected B-V and agglomerate kinetics. Distributions of reactant gas, liquid water and heat within the cell are investigated. The expressions for the relationship between the liquid water saturation on each electrode and current density, as well as the liquid water saturation between anode and cathode, are regressed.

2. Model description

2.1 Assumption

Some additional assumptions were employed in this work in addition to those in the previous papers [35-39]:

1. Steady state, two-phase flow, along the channel model of a PEMFC.
2. Gas flow in the channels is laminar flow and incompressible.
3. Reactant gases enter the gas channels in a direction normal to the channel cross section.
4. Liquid water saturation in channels is continuous.
5. Gas diffusion layers and catalyst layers are isotropic.
6. No liquid water enters the channels at the inlets.
7. Same electrodes and bipolar plates are used in the anode and cathode, respectively.

2.2 Governing equations

The conservation equations of mass, momentum, species, energy and charges are summarized as Eqns. (1) to (4):

$$\nabla \cdot (\rho^g \mathbf{u}^g) = S_m \tag{1}$$

$$\rho^g(\mathbf{u}^g\cdot\nabla\mathbf{u}^g)=\nabla\left[-pI+\mu^g\nabla\mathbf{u}^g+\mu^g(\nabla\mathbf{u}^g)^T-\frac{2}{3}\mu^g(\nabla\cdot\mathbf{u}^g)I\right] \quad (2)$$

$$\rho^g\mathbf{u}^g\cdot\nabla w_i^g-\nabla\cdot[\rho^g\sum_{j=1}^{N}(1-s')D_{ij}(\nabla x_j^g-w_j^g)\frac{\nabla p}{p}+D_i^T\frac{\nabla T}{T}]=M_iS_i^g \quad (3)$$

$$\nabla\cdot[\sum_{i=g,l}(\varepsilon\rho c_p\mathbf{u})_iT]-\nabla\cdot(\sum_{i=g,l,s}k_i\nabla T)=S_T \quad (4)$$

$$\sigma_s^{eff}\nabla\cdot\nabla\varphi_s+\sigma_M^{eff}\nabla\cdot\nabla\varphi_M=0 \quad (5)$$

where ρ (kg m^{-3}) is density, $\mathbf{u}$ (m s^{-1}) is velocity, p (Pa) is pressure, μ (Pa s) is viscosity, M (kg mol^{-1}) is molecular weight, D (m^2 s^{-1}) is diffusion coefficient, D^T (kg m^{-1} s^{-1}) is thermal diffusion coefficient, c_p (J mol^{-1} K^{-1}) is specific heat capacity, k (W m^{-1} K^{-1}) is thermal conductivity, T (K) is temperature, σ (S m^{-1}) is conductivity φ (V) is potential. w is mass fraction, x is mole fraction, ε is volume fraction, s' is corrected liquid water saturation and I is identity matrix. Subscript *i* and *j* represent species *i* and *j* and superscript *g* means gas phase. S is the source term, which is given in detail in Tables 1 to 3. Note that Eq. (1) to Eq. (3) were applied on reactant gas only and the gas velocity in porous electrodes could be related to pressure according to Darcy's law as below:

$$\mathbf{u}^g=-\frac{k_p}{\mu^g}\nabla p \quad (6)$$

where k_p (m^2) is the permeability of the porous media.

For the purpose of describing dissolved and liquid water transport, the following equations were used.

$$\nabla\cdot(n_d\frac{i_M}{F})-\nabla\cdot(D_{w-M}\nabla c_w^d)-\nabla\cdot(\frac{k_{p,M}c_w^d}{\mu_w}\nabla p)=S_w^d \quad (7)$$

$$\nabla\cdot(\rho_w^lD_c\nabla s-\frac{\rho_w^lk_r^l\mu_w^g}{k_r^g\mu_w^l}\mathbf{u}^g)=M_wS_w^l \quad (8)$$

Eq. (7) was developed by applying the diffusive approach to a conservation equation of dissolved water, while Eq. (8) was obtained by applying the volume average approach to the continuity equation

and using Darcy's law for both the liquid and gas phases.

The capillary diffusion coefficient, D_c ($m^2\ s^{-1}$), was calculated using Eq. (9) [32]:

$$D_c = -\frac{k_r^l}{\mu_w^l}\sigma\cos(\theta_c)(\varepsilon k_p)^{1/2}\frac{dJ(s)}{ds} \tag{9}$$

where k_r^l is the relative permeability of liquid phase, μ_w^l (Pa s) is the dynamic viscosity of liquid water, σ ($N\ m^{-1}$) is the surface tension, θ_c (°) is the contact angel, ε is the porosity of the electrode, k_p (m^2) is the permeability of the porous electrode, $J(s)$ is the Leverett function.

The equilibrium membrane/ionomer water content, determined based on water uptake measurement, is given as [33]:

$$\lambda^{eq} = 16.8s + 14.0(1-s) \qquad s > 0 \tag{10}$$

The permeability of gas channels was calculated by Hagen-Poiseuille equation [34].

$$k_{p,ch} = \frac{c_{sf} d_h^2}{32} \tag{11}$$

where c_{sf} is the flow shape factor (1.127 for a square cross-section) and d_h is the hydraulic diameter of a channel, which can be calculated by the relation of the cross-sectional area and wetted perimeter.

The electrochemical reactions inside the catalyst layers according to three different mechanisms, including B-V, (1-s) corrected B-V and agglomerate assumption, can be written as below:

$$i_{BV} = a_{agg}^M i_{0,i}^{ref}\left(\frac{p_i}{c_i^{ref} H_i}\right)^{\gamma}\left[\exp\left(\frac{-\alpha_{Rd,i}F\eta_i}{RT}\right) - \exp\left(\frac{\alpha_{Ox,i}F\eta_i}{RT}\right)\right] \tag{12}$$

$$i_{(1-s)BV} = (1-s)a_{agg}^M i_{0,i}^{ref}\left(\frac{p_i}{c_i^{ref} H_i}\right)^{\gamma}\left[\exp\left(\frac{-\alpha_{Rd,i}F\eta_i}{RT}\right) - \exp\left(\frac{\alpha_{Ox,i}F\eta_i}{RT}\right)\right] \tag{13}$$

$$i_{agg} = nF\left(\frac{p_i}{c_i^{ref} H_i}\right)^{\gamma}\left[\frac{1}{E_{agg}k_{agg}} + \frac{(r_{agg}+\delta_M+\delta_w)}{r_{agg}}\left(\frac{\delta_M}{a_{agg}^M D_{O_2-M}} + \frac{\delta_w}{a_{agg}^w D_{O_2-w}}\right)\right]^{-1} \tag{14}$$

where

$$k_{agg} = \frac{a_{agg}^{M} i_{0,i}^{ref}}{nF}\left[\exp(\frac{-\alpha_{Rd,i}F\eta_i}{RT}) - \exp(\frac{\alpha_{Ox,i}F\eta_i}{RT})\right] \quad (15)$$

The subscript i is for anode and cathode, respectively, and the superscript γ equals to 0.5 for hydrogen oxidation reaction (HOR) in anode and 1.0 for ORR in cathode. The properties of the catalyst layer (porosity, specific area, ionomer and water film thickness), gas transport through the porous electrode (species diffusion in gas mixture and Knudsen diffusion), numerous key parameters and fundamental equations, were listed in Table 4. Details can be found in literature [35-39].

2.3 Boundary conditions

At anode inlet (A'-B') and cathode inlet (G-H) as shown in Fig. 1, the temperature, mole fractions of reactant gases in gas mixture, and liquid water saturation are given as below:

$$T = T^{cell},\ x_{w,a}^{0} = \frac{p_{sat}RH_a}{p_a},\quad x_{H_2}^{0} = 1 - x_{H_2O,a,in},\quad s_a = 0 \quad (16)$$

$$T = T^{cell},\ x_{w,c}^{0} = \frac{p_{sat}RH_c}{p_c},\ x_{O_2}^{0} = 0.21(1 - x_{H_2O,c,in}),\ x_{N_2}^{0} = 0.79(1 - x_{H_2O,c,in}),\ s_c = 0 \quad (17)$$

The gas velocities at the inlets of both electrodes are related to their stoichiometry shown as follow:

$$\mathbf{u}_a^{g,0} = \frac{\xi_a RTi^{ref} A_M}{2Fp_a x_{H_2} A_{ch}},\quad \mathbf{u}_c^{g,0} = \frac{\xi_c RTi^{ref} A_M}{4Fp_c x_{O_2} A_{ch}} \quad (18)$$

where i^{ref} is the reference current density (defined as 1.0 A cm^{-2} in this study), ξ_a and ξ_c are the stoichiometry of the anode and cathode, respectively. A_M (m^2) and A_{ch} (m^2) are the effective area of electrode and the cross-sectional area of channel, respectively.

At the inlet and outlet of both the anode and cathode, the pressure was given as a boundary condition.

$$p_a = p_a^0,\ p_c = p_c^0 \quad (19)$$

The water content on the CL-membrane interfaces of anode (C-C') and cathode (F-F') were defined as Dirichlet boundaries with the values according to the following equations [14, 37-39]:

$$\lambda = 0.043 + 17.81\alpha_w - 39.85\alpha_w^2 + 36.0\alpha_w^3 \quad (20)$$

$$\alpha_w = x_w \frac{p}{p_{sat}} + 2s \quad (21)$$

2.4 Numerical solution

The numerical solution of the fully coupled governing equations was based on the finite element method (FEM). First of all, mesh was developed over the computational domain by dividing it into numerous elements. The distance between each element is known as the step. At each step, the equations accounting for different phenomena were fully coupled and computed with the boundary conditions. Initial value was given to each parameter at the first attempt then followed by an iterative process until the calculation error was smaller than 10^{-5}. Commercial software COMSOL Multiphysics 4.4 was used to implement the fully coupled equations. The key to successfully solving this model is simulating the membrane/ionomer water content, which significantly affects many critical parameters, i.e. ionomer volume fraction, EOD coefficient, ionic conductivity, hydraulic permeability and water diffusivity.

2.5 Mesh independence

Theoretically, the computation error in the solution related to the grid must disappear for an increasingly fine mesh. The effect of mesh on the final simulation results is more significant at high current density due to the increasing impact of mass transport. The current density at a low cell voltage (0.2 V) was therefore taken as the parameter to evaluate nine mesh grids (see Table 5) and determine the influence of the element number on the solution. In this study, the number of elements on various computational domains, including flow channel, GDL, CL and membrane, was investigated with a fixed number of elements (250) along the channel [36]. Three levels of element numbers were studied in each domain, which guaranteed the total number of element increasing at

1×10^4 each time. Fig. 2 shows that the current density reaches an asymptotic value while the computation duration increases as the number of elements increases. The current density almost kept as a constant when a finer mesh as Grid 7 was applied. A relative rapidly increase in computational duration was observed from Grid 5 to Grid 7. This indicated that the time consuming step among the computational process was in the catalyst layers, in which numbers of transport and electrochemical processes were involved. In order to reduce the calculation error, finer mesh has to be developed on catalyst layers. Having balancing both the computational accuracy and duration, Grid 6 was selected considering a sufficient reliability to ensure mesh independence with acceptable calculating time.

3. Results and discussions

3.1 Model validation

Fig. 3 shows the comparison of the simulation results with experimental data obtained both in-house and selected from literature [41]. For the in-house case shown in Fig. 3(a), the anode and cathode catalyst layers were made from 20% Pt/C with a Pt loading of 0.1 and 0.4 mg cm^{-2}, respectively. 5% Nafion® ionomer solution in de-ionized water was used as binder. The ionomer mass ratios were 20% in the catalyst layers at both the anode and cathode. Nafion® 112 membrane was used as electrolyte sandwiched between anode and cathode. The graphite plates with an active area of 1.0 cm × 1.0 cm were grooved with serpentine gas channels with a dimension of 0.1 cm × 0.1 cm. For the case in Fig. 3(b), 40% Pt/C with a platinum loading of 0.4 mg cm^{-2} was used. Serpentine flow field was applied as well with a dimension of the 0.1 cm × 0.1 cm and an active area of 7.2 cm × 7.2 cm. For the formal case, the cell was tested with the cell and gas inlet temperatures at 80 °C under a hydrogen flow rate of 200 sccm at the anode side and an air flow rate of 500 sccm at the cathode side. For the latter case, cell and gas inlet temperatures were 70 °C with the hydrogen flow rate of 1200

sccm and air flow rate of 2200 sccm. Reactant gas pressure and humidity were kept at 1.0 atm and 100% for both cases. The parameters used for model validation and base case in this study are listed in Table 6. The cathode transfer coefficient (α_c) was obtained by fitting the experimental polarisation curves in the kinetics control zone (cell voltage higher than 0.8 V) and the obtained α_c was further verified by the Tafel slope worked out in the model [40]. More details of the membrane electrode assembly (MEA) preparation and cell test can be found elsewhere [37-39, 41].

A good agreement between the simulation results and the experimental data is indicated by Fig. 3 at higher cell voltages, corresponding to lower current densities, due to the slow reaction rate and insignificant mass transport impact. There was a typical drop in cell voltage due to various losses in terms of activation polarization loss, ohmic loss and concentration polarization loss, as the current density increased. A more rapid drop in current density, caused by the increasing mass transport resistance, was observed at high current densities (mass transport control zone), where the departures of simulation results compared with experimental data was clearly observed. The rapid decrease in current density can be explained by the increase in mass transfer losses due to the oxygen diffuses to and then adsorbs on catalyst surface to perform electrochemical reactions, which is determined by both the electrode structure and the reactant provided, e.g. the mole fraction of oxygen against nitrogen and water vapor in air at the cathode side. When the balance between diffusion and consumption rates is achieved, a limit current density is reached. The formation of liquid water inside the electrode void space restricts oxygen diffusion, especially if it is accumulated liquid water near the downstream channel. However, the 2D model in this study failed to fully represent the whole MEA, leading to an under-estimation of the impact of mass transfer losses in the downstream channel. Especially for a large active area in the case of Wang [41], the departure of simulation result and

experimental data is more apparent.

3.2 Comparison of different mechanisms

Three models of describing the effect of liquid water generation were compared, based on the polarization curves, through the reaction mechanism: traditional B-V, (1-s) corrected B-V and agglomerate models. The results are shown in Fig. 4 and the channel lengths are 1 and 10 cm in Fig. 4(a) and Fig. 4(b), respectively. The current density predicted using (1-s) corrected B-V model was slightly lower than that by traditional B-V model in the full range of cell voltage. Compared with Fig 3, we can see that the agglomerate model is in better agreement with the experimental results, while the (1-s) corrected B-V model still shows limitations in describing the significant mass transport resistance at high current density. This is because the cell performance at high current density is determined by mass transport rather than electrochemical kinetics. Even through the predicted current densities are deduced by considering the partial occupation of platinum active site by liquid water, the (1-s) corrected B-V model fails to take the gas diffusion resistance through the ionomer film into account. More rapid drop in current density was observed at high current densities in Fig. 4(b) in comparison with that in Fig. 4(a), which indicated that the impact of mass transport on cell performance at high current densities was more pronounced for long flow channels than for short channels. This can be explained by the larger fuel concentration gradient and more liquid water accumulation in the downstream channel. It is also clear, due to slow reaction rate and low mass transport impact at low current densities, the results predicted by the agglomerate model were very close to that of B-V model. However, the agglomerate model is capable of capturing the impact of mass transport at high current densities by considering the species transport resistance through the ionomer and liquid water films surrounding agglomerates.

3.3 Distributions of reactant gases

The mole fractions of hydrogen and oxygen within electrode and flow channel at various current densities from 0.2 to 1.4 A cm^{-2} are shown in Fig. 5. It is clear the concentrations of both hydrogen and oxygen decrease along the diffusion direction and the concentration gradient is more apparent at high current densities. Hydrogen consumption near the anode outlet is observed from the distribution of hydrogen mole fraction shown in Fig. 5(a). This can be explained by the electrochemical reaction and the effect of electro-osmotic drag (EOD), especially at high current densities. The increase in current density from 0.6 to 1.0 A cm^{-2} leads to a 69% increase in the rate of hydrogen consumption by HOR and a 63% increase in the water flux under the driving force of EOD. In comparison with hydrogen concentration distribution in flow channel, Fig. 5(b) indicates that, oxygen remains at a very high concentration close to the inlet level in flow channel, in the full range of current densities from 0.2 to 1.4 A cm^{-2}, along the air flow direction. On the contrary, a significant concentration gradient is shown through the diffusion direction as the current density increases, which is in consistence with the previous modelling results of Nguyen et al. [42]. This can be explained by the increase in oxygen consumption due to the accelerated ORR and the presence of large oxygen transport resistance through the electrode. In addition, the more water generated at high current density dilutes the oxygen. The formation of liquid water reduces the porosity of the electrode and increases the thickness of liquid water film surrounding the agglomerate, leading to a further decrease in the oxygen diffusivity through the electrode before it can reach the active sites. However this does not happen at the anode side due to the much easier diffusion of the smaller hydrogen molecular and its relative high mole fraction.

3.4 Distributions of effectiveness factor

316 The effectiveness factors, used to evaluate how effective the catalyst layer is utilized, of the ACL
317 and CCL at various current densities from 0.3 to 1.2 A cm^{-2} are shown in Fig. 6. In Fig. 6(a), X=0 and
318 X=1 represent the interfaces of GDL-CL and CL-membrane of anode, while Y=0 and Y=1 represent
319 the anode inlet and outlet, respectively. In Fig. 6(b), X=0 and X=1 represent the interfaces of
320 membrane-CL and CL-GDL of cathode, while Y=0 and Y=1 represent the cathode outlet and inlet,
321 respectively. The highest effectiveness factors, for both the ACL and CCL, are observed at 0.3 A cm^{-2},
322 which decrease with the increase of the current density to 1.2 A cm^{-2}. The decrease in effectiveness
323 factor can be explained by the increased electrochemical reaction rate as the current density increases.
324 At this stage, the overall reaction rate is mainly determined by the rate of chemical reaction rather
325 than mass transport. As the current density increases, the increase in electrochemical reaction rate
326 leads to a faster consumption of reactant gases relative to the diffusion rate to the active sites. The rate
327 determining process therefore changes from the electrochemical reaction to the reactant gas diffusion.
328 Consequently, along the gas diffusion direction through catalyst layers, the catalyst utilization is
329 higher near the GDL-CL interface (X=0 for anode and X=1 for cathode) than that of the
330 CL-membrane interface (X=1 for anode and X=0 for cathode), which agree with the finding of Sun et
331 al. [26]. It is important to note that the change of the effectiveness factor is not pronounced along the
332 reactant gas flow direction (Y direction). This is because the gases are supplied above stoichiometric
333 requirements. Reactant gases are provided at such rates to guarantee the almost uniform
334 concentrations along the channels. A comparison of Fig. 6(a) and Fig. 6(b) shows a much higher
335 effectiveness factor of ACL than that of CCL, especially at high current densities. The ACL
336 effectiveness factor remains high, ca. 80%, for a certain distance along the hydrogen diffusion. On the
337 contrary, due to the large oxygen transport resistance through the cathode, the effectiveness factor of

CCL is much lower compared with that of ACL. The platinum catalyst in the CCL located near the CL-GDL interface cannot be fully utilized, resulting in a waste of expensive catalyst.

3.5 Distributions of current density

Fig. 7 shows the current density distributions within the catalyst layers of anode and cathode at various cell voltages from 0.7 to 0.4 V. The current densities increase in both catalyst layers as the cell voltage decreases. It can be seen that the current densities decrease along the reactant gas diffusion direction at both the anode and cathode, leading to insufficient utilization of the catalyst near the CL-membrane boundary (X=0 for cathode and X=1 for anode). On the contrary, the current densities almost remain constant along the reactant flow direction. It is apparent that the current density distribution in the ACL is more uniform than that in the CCL. In the region near the CL-membrane interface, the anode current density is higher than the cathode current density at a fixed cell voltage. This can be explained by the sluggish ORR in the cathode. Due to the slower ORR in the cathode, the interior of the cathode catalyst layer is not fully utilised, especially at a high current density.

3.6 Distributions of liquid water saturation

The liquid water saturations in both electrodes, including CLs and GDLs, are shown in Fig. 8. The coordinates of X and Y indicate the same geometry as those in Fig. 6. It is clear that the liquid water saturation increases in both electrodes as the current density increases. Also, the liquid water saturation is relatively high near the outlets in both electrodes, indicating more severe water flooding in these areas. This finding is in consistence with the experimental measurement of o et al. [20]. Comparison of Fig. 8(a) and Fig. 8(b) shows that the gradient of liquid water saturation is greater in cathode electrode than of the anode, especially along the channel direction.

3.7 Distributions of temperature

The temperature profiles at various current densities from 0.6 to 1.0 A cm^{-2} are shown in Fig. 9. A non-uniform temperature distribution is clearly indicated. The temperature increases along the air flow and decreases from the cathode to the anode through the membrane with the highest value at the cathode side. The most significant temperature rise, as expected, is observed in the cathode, leading to a ca. 4 °C difference between anode and cathode at 1.0 A cm^{-2}. This temperature increase at the cathode can be explained by both the exothermic ORR and water phase-transfer occurred. The latter comprises ca. 6% of the total heat released at 1.0 A cm^{-2} (Table 7), which is the latent heat associated with water phase change from dissolved water to liquid water during membrane/ionomer desorption. A temperature rise along the cathode flow channel is clearly shown in Fig. 9. This can be explained by the heat released by water phase-transfer as liquid water is pushed downstream to the channel exit by the airflow.

As a main heat source, the heat released by ORR comprises more than 90% of the total heat released at 1.0 A cm^{-2}. Similar to the ORR in the cathode, the HOR in the anode occupies more than 88% of the total heat change, which therefore can be considered as the main heat source in the anode. Due to the endothermic nature and large contribution of the HOR to the total heat in the anode, the anode is endothermic in full range of current densities. With the increase in current density, the ratio of HOR to the total heat in the anode increases whereas that of ORR to the total heat in the cathode decreases. In the anode, the heat released by ionomer water uptake is the second main heat source, which comprises ca. 10% of the total heat in the anode at 0.2 A cm^{-2}. As the current density increases, there is a decrease in the contribution of the heat released by ionomer water uptake in the anode. This is caused by a relative fast increase in the heat absorption due to the HOR. Although the absolute heat

382 released by ionomer water uptake increases, the ratio decreases from ca. 11% to 3% as the current
383 density increases from 0.2 to 1.0 A cm^{-2}. Table 7 also shows that the heat contribution of ORR
384 decreases and ionomer desorption increases with the increase in current density in the cathode. This is
385 because more dissolved water is generated at a high current density, which then transfers to liquid
386 water by ionomer desorption after the ionomer is fully saturated.

387 The detailed temperature profiles at the anode channel-GDL interface are shown in Fig. 10. The
388 temperature increases sharply along the hydrogen flow direction until a maximum temperature is
389 achieved, then slightly decreases near the anode outlet. The maximum temperature is located in the
390 middle of the channel near to the inlet. The temperature rise in the anode is much less than that of the
391 cathode due to the endothermic HOR within the anode catalyst layer (Fig. 9). This increase can be
392 explained by the heat transferred from the cathode and the latent heat released via water
393 phase-transfer. As shown in Table 7, the heat via water phase-transfer approximately comprises 11%
394 of total heat in the anode at 0.2 A cm^{-2}, which decreases to less than 3% as the current density
395 increases to 1.0 A cm^{-2}. Therefore, heat transfer from the cathode is the main heat source contributed
396 to the temperature rise in the anode.

397 3.8 Comparison of the isothermal and non-isothermal model

398 Fig. 11 shows the liquid water saturation at the cathode CL-GDL interface at 1.0 A cm^{-2} simulated
399 by both the isothermal and non-isothermal models. The dimensionless coordinate is the same as in Fig.
400 1. The liquid water saturation increases along the air flowing direction at the cathode GDL-CL
401 interface. By taking the temperature rise into account, the liquid water saturation predicted by the
402 non-isothermal model is slightly smaller than that by the isothermal model, caused by the fast increase
403 in the saturation pressure of water vapour (p_{sat}) with temperature. Specifically, p_{sat} increases from

31.16 to 36.99 kPa as temperature increases from 70 to 74 °C. The increase in the saturation pressure of water vapour, improves the water carrying capacity (WCC) of gas mixture, thus to a certain extent, prohibits the water phase-transfer from vapour to liquid water. Furthermore, the temperature rise is more apparent at a high operating temperature in comparison with a low one [38]. The heat released during fuel cell operation can help mitigate water flooding by improving the WCC of the reactant gases. However, this is at the expense of reducing the effective oxygen concentration of the cathode reactant gas, which may results in a more significant decline in cell performance than that induced by flooding. The mole fraction of oxygen in a fully humidified mixture decreases from 18.24% to 13.34% as temperature increases from 70 to 74 °C, which may lead to oxygen starvation and damage to the cathode. Thus, for a fuel cell operated at a high temperature, the performance may be limited by the excessive moisture in the cathode reactant gas.

3.9 Regressed expressions for liquid water saturation

Fig. 12 shows the liquid water saturation in both electrodes (including CLs and GDLs) at various current densities. It indicates that the increase of the current density leads to a logarithmic increase in the liquid water saturation, which is greater in the cathode than that in the anode. In addition, the liquid water saturations are slightly larger in CLs than that in GDLs at both electrodes, especially in the cathode due to the water generated via ORR.

Mathematical expressions are regressed in terms of logarithmic and exponential equations to fit the average liquid water saturation in both electrodes, as shown in Fig. 13, respectively. Linear logarithmic transform function (Log3P1) and two-phase exponential decay function with time offset (ExpDecay2) were selected as regression functions. The cathode average liquid water saturation (s_c) in Fig. 13(a) could be well fitted by a logarithmic expression (Eq. 22) with a R^2 coefficient of 99.33%.

(R^2 is a statistical measure of how close the data to the fitted regression line). However, a large error of fitting occurs in medium and high current densities when applying the same regression function to the anode average liquid water saturation (s_a). The logarithmic expression (Eq. 23) led to a R^2 coefficient of only 94.26% and a remarkable standard error of parameter c. Thus, the logarithmic expression of s_a - i was considered as an unconfident relationship without enough accuracy. Instead, an exponential expression (Eq. 24), more complex in form in comparison with logarithmic expression, is regressed in Fig. 13(b). It can be seen that the exponential express is more accurate here.

$$s_c = 0.1344 + 0.05912\ln(i + 0.15109) \quad (R^2 > 99.33\%) \tag{22}$$

$$s_a = 0.07405 + 0.01354\ln(i + 3.00567\times10^{-4}) \quad (R^2 > 94.26\%) \tag{23}$$

$$s_a = 0.10232 - 0.06965\exp(-\frac{i + 0.00489}{1.12255}) - 0.0378\exp(-\frac{i + 0.00489}{0.02805}) \quad (R^2 > 99.88) \tag{24}$$

The average liquid water saturations in both electrodes with respect to the current density higher than 0.6 A cm^{-2} are shown in Fig. 14. Log3P1 function, which is used to fit the data plotted, results in accurate expressions (Eq. 25 and Eq. 26) with R^2 greater than 99.9% in both electrodes. This indicates that the changes in the average liquid water saturation in both electrodes follows a logarithmic relationship at current densities higher than 0.6 A cm^{-2}. Comparing Fig. 14 with Fig. 13(b) suggests that, as the current density increases, the increase in the average liquid water saturation in the anode firstly obeys exponential function at low current densities followed by logarithmic function at high current densities. However, it is insufficient to describe the relationship between the anode average liquid water saturation and current density using a logarithmic function in full range of current densities.

$$s_c = 0.11463 + 0.07763\ln(i + 0.40119) \quad (R^2 > 99.99\%) \tag{25}$$

$$s_a = 0.06909 + 0.02897\ln(i + 0.16568) \quad (R^2 > 99.90\%) \tag{26}$$

448 The relationship between average liquid water saturation in the anode and the cathode is regressed
449 in Fig. 15. The data plotted can be roughly divided into three segments, corresponding to the liquid
450 water saturation at the low, medium and high levels. In order to guarantee the accuracy, the R^2
451 coefficient of each regression expression within each segment is controlled greater than 99.9%. The
452 results indicate that at the low and high liquid water saturation, a linear relationship exists between the
453 average liquid water saturations in the anode and the cathode. However, at the medium liquid water
454 saturation, the exponential function is more accurate than the linear relationship. The relation of liquid
455 water saturation at the anode and cathode is similar to the modelling results of Jiang and Wang [43].
456 As stated by O'Rourke et al. [21], the water flooding in anode could be detected prior to severe
457 damage of cathode catalyst, which could be avoided with the aid of the regressed expressions of the
458 liquid water saturation in the anode and the cathode.

459 $$s_c = 3.65764 s_a - 1.45542 \times 10^{-4} \quad (R^2 > 99.99\%) \quad \text{low water saturation} \qquad (27)$$

460 $$s_c = \exp(27.0888 s_a^2 + 31.24035 s_a - 4.00174) \quad (R^2 > 99.44\%) \quad \text{medium water saturation} \qquad (28)$$

461 $$s_c = 2.32873 s_a - 0.03044 \quad (R^2 > 99.96\%) \quad \text{high water saturation} \qquad (29)$$

462 # 4. Conclusion

463 A two-dimensional, two-phase flow, along-the-channel, non-isothermal, CFD model for a single
464 PEMFC is developed. Water was treated as three different phases: vapour, dissolved and liquid water.
465 The water phase-transfer between each phase, associated with the combinational transport mechanism
466 through the membrane, is numerically studied. Three types of models are compared for hydrogen
467 reduction and oxygen oxidation in catalyst layers, including traditional B-V, (1-s) corrected B-V and
468 agglomerate mechanism. Temperature changes in MEA and channels due to electrochemical reaction,
469 ohmic resistance and water phase change are analysed and the contribution of each heat source is

summarised and compared at a variety of current densities. Mathematical expressions for liquid water saturations against current density at both anode and cathode are regressed and the mathematical relationship between them is developed. Analysis of the simulation results leads to the following insights:

The current density predicted by traditional B-V, (1-s) corrected B-V and agglomerate models are in general agreement with experimental data at low current densities. As the current density increases, by accounting for the extra oxygen diffusion resistance through the ionomer/water film and the loss of catalyst layer porosity due to ionomer swelling, the agglomerate model gives more accurate simulation results in comparison with the others. However, due to significant water flooding in downstream channel, the 2D model developed cannot fit the experimental data very well at high current densities, especially when long flow channels are applied. Due to the more significant transport resistance of oxygen in the cathode than that of hydrogen in the anode, the effectiveness factor of the cathode catalyst layer is much lower than that of the anode catalyst layer.

Water flooding, represented by the liquid water saturation, is prone to occur near the downstream channel of both the anode and cathode. Liquid water saturation is temperature dependent, which requires the non-uniform distribution of temperature predicted by the non-isothermal model. The most significant temperature rise is in the cathode catalyst layer due to the contribution of exothermic ORR, which comprises more than 90% of total heat released. With the increase in the current density, the heat contribution of ORR decreases while ionomer/membrane desorption increases. On the contrary, the endothermic HOR is the main heat source in the anode. At a low current density, the heat released by ionomer/membrane water uptake contributes ca. 10% to the total heat in the anode.

The mathematical expressions for the relationship between the current density and liquid water

saturations in both the anode and the cathode are regressed. Nonlinear current density – water saturation relations are found at both electrodes. It is believed that the liquid water saturation in the cathode presents logarithm relevant to current density. However, the liquid water saturation in the anode increases exponentially as the current density increase. At a high current density greater than 0.6 A cm^{-2}, the liquid water saturations at both electrodes can be described by logarithmic relationship. The relationship between liquid water saturations in the anode and the cathode is also regressed. It is found that at low and high current densities, the relationship can be accurately represented by linear function, but exponential function is believed to be more accurate at medium current densities.

Acknowledgements

The authors gratefully acknowledge the financial support from the EPSRC Supergen Fuel Cell Consortium award no G030995.

References

[1] Gottesfeld S. Fuel cell techno-personal milestones 1984-2006. J Power Sources 2007;171:37-45.

[2] Dai W, Wang H, Yuan XZ, Martin JJ, Yang D, Qiao J, Ma J. A review on water balance in the membrane electrode assembly of proton exchange membrane fuel cells. Int J Hydrogen Energy 2009;34:9461-78.

[3] Wang Y, Chen KS, Mishler J, Cho SC, Adroher XC. A review of polymer electrolyte membrane fuel cells: Technology, applications, and needs on fundamental research. App Energy 2011;88:981-1007.

[4] Wang J. Barriers of scaling-up fuel cells: Cost, durability and reliability. Energy 2015;80:509-21.

[5] Lund H, Andersen AN, Østergaard PA, Mathiesen BV, Connolly D. From electricity smart grids to smart energy systems – A market operation based approach and understanding. Energy 2012;42:96-102.

[6] Rokni M. Thermodynamic and thermoeconomic analysis of a system with biomass gasification, solid oxide fuel cell (SOFC) and Stirling engine. Energy 2014;76:19-31.

[7] Cappa F, Facci AL, Ubertini S. Proton exchange membrane fuel cell for cooperating households: A convenient combined heat and power solution for residential applications. Energy 2015;90:1229-38.

[8] Carton JG, Olabi AG. Wind/hydrogen hybrid systems: Opportunity for Ireland's wind resource to provide consistent sustainable energy supply. Energy 2010;35:4536-44.

[9] Djilali N. Computational modelling of polymer electrolyte membrane (PEM) fuel cells: Challenges and opportunities. Energy 2007;32:269-80.

[10] Bazylak A. Liquid water visualization in PEM fuel cells: A review. Int J Hydrogen Energy 2009;34:3845-57.

[11] Carton JG, Lawlor V, Olabi AG, Hochenauer C. Zauner G. Water droplet accumulation and motion in PEM (Proton Exchange Membrane) fuel cell mini-channels. Energy 2012;39:63-73.

[12] Ge S, Li X, Yi B, Hsing IM. Absorption, desorption, and transport of water in polymer electrolyte membranes for fuel cells. J Electrochem Soc 2005;152:A1149-57.

[13] Wu H, Berg P, Li X. Steady and unsteady 3D non-isothermal modeling of PEM fuel cells with the effect of non-equilibrium phase transfer. App Energy 2010;87:2778-84.

[14] Yang XG, Ye Q, Cheng P. Matching of water and temperature fields in proton exchange membrane fuel cells with non-uniform distributions. Int J Hydrogen Energy 2011;36:12524-37.

[15] Djilali N. Computational modelling of polymer electrolyte membrane (PEM) fuel cells: Challenges and opportunities. Energy 2007;32:269-80.

[16] Das PK, Li X, Liu ZS. Analysis of liquid water transport in cathode catalyst layer of PEM fuel cells. Int J Hydrogen Energy 2010;35:2403-16.

[17] Meng H, Wang CY. Model of Two-Phase Flow and Flooding Dynamics in Polymer Electrolyte Fuel Cells. J Electrochem Soc 2005;152:A1733-41.

[18] Ferreira RB, Falcao DS, Oliveira VB, Pinto AMFR. Numerical simulation of two-phase flow in

542 an anode gas channel of a proton exchange membrane fuel cell. Energy 2015;82:619-28.

543 [19] Wong KH, Loo KH, Lai YM, Tan SC, Tse CK. A theoretical study of inlet relative humidity
544 control in PEM fuel cell. Int J Hydrogen Energy 2011;36:11871-85.

545 [20] Iranzo A, Boillat P, Biesdorf J, Salva A. Investigation of the liquid water distribution in a 50 cm2
546 PEM fuel cell: Effects of reactants relative humidity, current density, and cathode stoichiometry.
547 Energy 2015;82:914-21.

548 [21] O'Rourke J, Ramani M, Arcak M. In situ detection of anode flooding of a PEM fuel cell. Int J
549 Hydrogen Energy 2009;34:6765-70.

550 [22] Anderson R, Blanco M, Bi X, Wilkinson DP. Anode water removal and cathode gas diffusion
551 layer flooding in a proton exchange membrane fuel cell. Int J Hydrogen Energy 2012;37:
552 16093-103.

553 [23] Wang ZH, Wang CY, Chen KS. Two-phase flow and transport in the air cathode of proton
554 exchange membrane fuel cells. J Power Sources 2001;94:40-50.

555 [24] He G, Ming P, Zhao Z, Abudula A, Xiao Y. A two-fluid model for two-phase flow in PEMFCs. J
556 Power Sources 2007;163:864-73.

557 [25] Ferreira RB, Falcao DS, Oliveira VB, Pinto AMFR. A one-dimensional and two-phase flow
558 model of a proton exchange membrane fuel cell. J Chem Technol Biotechnol 2015; 90:1547-51.

559 [26] Sun W, Peppley BA, Karan K. An improved two-dimensional agglomerate cathode model to
560 study the influence of catalyst layer structural parameters. Electrochim Acta 2005;50:3359-74.

561 [27] Shah AA, Kim GS, Sui PC, Harvey D. Transient non-isothermal model of a polymer electrolyte
562 fuel cell. J Power Sources 2007;163:793-806.

563 [28] Ju H, Meng H, Wang CY. A single-phase, non-isothermal model for PEM fuel cells.
564 International J Heat and Mass Transfer 2005;48:1303-15.

565 [29] Wang MH, Guo H, Ma CF. Temperature distribution on MEA surface of a PEMFC with
566 serpentine channel flow bed. J Power Sources 2006;157:181-7.

567 [30] Zhang GS, Guo LJ, Ma LZ, Liu HT. Simultaneous measurement of current and temperature

distributions in a proton exchange membrane fuel cell. J Power Sources 2010;195:3597-604.

[31] Lin H, Cao TF, Chen L, He YL, Tao WQ. In situ measurement of temperature distribution within a single polymer electrolyte membrane fuel cell. Int J Hydrogen Energy 2012;37:11871-86.

[32] Pasaogullari U, Wang CY. Two-phase transport and the role of microporous layer in polymer electrolyte fuel cells. Electrochim Acta 2004;49:4359-69.

[33] Wu H, Berg P, Li X. Modelling of PEMFC transients with finite-rate phase transfer processes. J Electrochem Soc 2010;157:B1-12.

[34] Wang CY, Groll M, Rosler JS, Tu CJ. Porous medium model for two-phase flow in mini channels with applications to micro heat pipes. Heat Recovery Syst CHP 1994;14:377-90.

[35] Xing L, Mamlouk M, Scott K. A two dimensional agglomerate model for a proton exchange membrane fuel cell. Energy, 2013;61:196-210.

[36] Xing L, Song X, Scott K, Picker V, Cao W. Multi-variable optimization of PEMFC cathodes based on surrogate modelling. Int J Hydrogen Energy 2013;38:14295-313.

[37] Xing L, Mamlouk M, Kumar R, Scott K. Numerical investigation of the optimal Nafion® ionomer content in cathode catalyst layer: An agglomerate two-phase flow modelling. Int J Hydrogen Energy 2014;39:9087-104.

[38] Xing L, Liu X, Alaje T, Kumar R, Mamlouk M, Scott K. A two-phase flow and non-isothermal agglomerate model for a proton exchange membrane (PEM) fuel cell. Energy 2014;73:618-34.

[39] Xing L, Das PK, Song X, Mamlouk M, Scott K. Numerical analysis of the optimum membrane/ionomer water content of PEMFCs: The interaction of Nafion® ionomer content and cathode relative humidity. Appl Energy 2014;138:242-57.

[40] Barbir F. PEM fuel cells: theory and practice. 1st ed. Oxford: Elsevier Academic Press; 2005.

[41] Wang L, Husar A, Zhou T, Liu H. A parametric study of PEM fuel cell performances. Int J Hydrogen Energy 2003;28:1263-72.

[42] Nguyen PT, Berning T, Djilali N. Computational model of a PEM fuel cell with serpentine gas flow channels. J. Power Sources 2004;130:149-57.

[43] Jiang F, Wang C-Y. Numerical modeling of liquid water motion in a polymer electrolyte fuel cell.

595 Int J Hydrogen Energy 2014;39:942-50.

596 # Nomenclature

A_s	reaction surface area per unit platinum mass, $m^2\ kg^{-1}$
a	specific area, m^{-1}
$c_{p,i}$	specific heat capacity of species i, $J\ mol^{-1}\ K^{-1}$
c	concentration, $mol\ m^{-3}$
D	diffusivity, $m^2\ s^{-1}$
D_c	capillary diffusion coefficient, $m^2\ s^{-1}$
D_{ij}	Maxwell-Stefan diffusion coefficient matrix, $m^2\ s^{-1}$
E	effectiveness factor
E^0	open circle potential, V
E_{cell}	cell voltage, V
EW	equivalent weight of Nafion® membrane, $g\ mol^{-1}$
F	Farady's constant, 96485 $C\ mol^{-1}$
f	platinum mass ratio to *Pt/C*
H	Henry's constant, $Pa\ m^3\ mol^{-1}$
i	current density, $A\ m^{-2}$
i_0	exchange current density, $A\ m^{-2}$
$J(s)$	Leverett function
k	rate coefficient, s^{-1}
k_i	Thermal conductivity of species i, $W\ m^{-1}\ K^{-1}$
k_r	relative permeability

k_p	hydraulic permeability, m^2
l	thickness, m
L	volume fraction
M_j	molecular weight for specie j, kg mol^{-1}
M_T	Thieles's modulus
m	mass loading, mg cm^{-2}
N	number per volume, m^{-3}
n	number
p	pressure, Pa
R	ideal gas constant, 8.314 J mol^{-1} K^{-1}
R_M	membrane resistance, Ω m^{-2}
RH	relative humidity
r	radius, m
S	source term
s	liquid water saturation
T	temperature, K
u	velocity vector, m s^{-1}
V	mole volume, m^3
w	mass fraction
X	normalised distance (x/δ_{CL})
x	mole fraction
Y	normalised distance ($z/(z_{CC}+ z_{Ch})$)

$\%M$	volume fraction of primary pores occupied by ionomer

597

598 *Greek*

α	charge transfer coefficient
α_w	water activity
λ	water content
μ	viscosity, Pa s
ρ	density, kg m^{-3}
ε	porosity
δ	thickness of ionomer/liquid water coating, m
γ	oxygen diffusion rate through the coating, s^{-1}
η	overpotential, V
σ	surface tension, N m^{-1}
θ_c	contact angel, °
σ_s	electronic conductivity, S m^{-1}
σ_M	ionic conductivity, S m^{-1}
φ	potential, V
Ψ_w	association parameter for water (the value is 2.6)

599 *Superscripts*

0	intrinsic
d	dissolved
eff	effective

ref	reference
eq	equilibrium
l	liquid
g	gas

Subscripts

a	anode
ads	adsorption
agg	agglomerate
C	carbon
c	cathode
CL	catalyst layer
des	desorption
GDL	gas diffusion layer
i	species i
j	species j
Kn	Knudsen diffusion
M	Membrane/ionomer
P	void space
Pt	platinum
Pt/C	platinum dispersed carbon
p	primary pores
r	relative

S	GDL penetration
s	secondary pores
T	temperature
w	liquid water
sat	saturation
tot	total
vl	vapour to liquid
vd	vapour to dissolved
dl	dissolved to liquid

601

602

603

604 Table 1 Conservation of water in different phases

605

	Channels	GDLs	CLs
Water vapour S_w^v	$-S_w^{vl}$	$-S_w^{vl}$	$-S_w^{vd}-S_w^{vl}$
Liquid water S_w^l	S_w^{vl}	S_w^{vl}	$S_w^{dl}+S_w^{vl}$
Dissolved water	0	0	$S_w^{r,i}+S_w^{vd}-S_w^{dl}$

606 Note: superscript *i* represents the anode or cathode, the unit for each source term is (mol m^{-3} s^{-1}).

607

608

609

610

611

612

613

614

615

616

617

618

619

620

621

622

Table 2 Conservation of heat

Membr	CLs	GDLs	Channels
S_T^M	$S_T^{dl} + S_T^{vl} + S_T^{wd} + S_T^{r,i} + S_T^{s,i} + S_T^M$	$S_T^{vl} + S_T^{s,i}$	S_T^{vl}

Note: superscript *i* represents the anode or cathode, the unit for each source term is (W m^{-3}).

645

646

647

648

649

650

651

652

653

654

655

656

657

658

659

660

661

662

663

664 Table 3 Source terms

Source terms	Unit	Domain
$S_m = M_{H_2} S_{H_2}^g + M_{O_2} S_{O_2}^g + M_w S_w^v$	kg m^{-3} s^{-1}	GDLs, CLs and channels
$S_{H_2}^g = \frac{i_a}{2F}$	mol m^{-3} s^{-1}	ACL

$S_{O_2}^{g} = \frac{i_c}{4F}$		mol m^{-3} s^{-1}	CCL
$S_w^{rc} = \frac{i_c}{2F}$		mol m^{-3} s^{-1}	CCL
$S_w^{vd} = k_{ads}(c_w^{eq} - c_w^{d})$	$c_w^{d} < c_w^{eq}$	mol m^{-3} s^{-1}	ACL and CCL
$S_w^{dl} = k_{des}(c_w^{d} - c_w^{eq})$	$c_w^{d} \geq c_w^{eq}$	mol m^{-3} s^{-1}	ACL and CCL
$S_T^{sa} = \frac{i_a^2}{\sigma_{GDL,a}^{eff}}$		W m^{-3}	Anode GDL
$S_T^{sc} = \frac{i_c^2}{\sigma_{GDL,c}^{eff}}$		W m^{-3}	Cathode GDL
$S_T^{M} = \frac{i_M^2}{\sigma_M^{eff}}$		W m^{-3}	Membrane, ACL and CCL
$S_T^{ra} = -\lvert i_a \rvert [\frac{T\nabla S_a}{2F}]$		W m^{-3}	ACL
$S_T^{rc} = \lvert i_c \rvert [\lvert \eta_c \rvert - \frac{T\nabla S_c}{4F}]$		W m^{-3}	CCL
$S_T^{vd} = M_w S_w^{vd} \nabla h_w^{vd}$		W m^{-3}	ACL and CCL
$S_T^{dl} = M_w S_w^{dl} \nabla h_w^{dl}$		W m^{-3}	ACL and CCL
$S_T^{vl} = M_w S_w^{vl} \nabla h_w^{vl}$		W m^{-3}	CLs, GDLs and channels
$S_w^{vl} = \begin{cases} k_{con}\frac{\varepsilon(1-s)x_w^g}{RT}(x_w^g p^g - p_{sat}) & x_w^g p^g \geq p_{sat} \\ k_{eva}\frac{\varepsilon s \rho_w^l}{M_w}(p_{sat} - x_w^g p^g) & x_w^g p^g < p_{sat} \end{cases}$		mol m^{-3} s^{-1}	CLs, GDLs and channels

Table 4 Expressions of key parameters

Description	Expression	Referen

		ce
Volume fraction of Pt/C	$L_{Pt/C} = \frac{m_{Pt}}{l_{CL}}\left(\frac{1}{\rho_{Pt}} + \frac{1-f}{f}\frac{1}{\rho_C}\right)$	[36]
Porosity of catalyst layer	$\varepsilon_{CL} = 1 - L_M - L_{GDL}(1-\varepsilon_{GDL}) - L_{Pt/C}$	[36]
Agglomerate density of catalyst layer	$N_{agg} = \frac{3L_{Pt/C}}{4(1-\varepsilon_{CL})\pi r_{agg}^{\ 3}}$	[36]
Specific area of agglomerate	$a_{agg} = \frac{m_{Pt}A_s}{l_{CL}}\frac{(1-\varepsilon_{CL})}{L_{Pt/C}}$	[36]
Reaction surface area per unit platinum mass	$A_s = (227.79f^3 - 158.57f^2 - 201.53f + 159.5)\times 10^3$	[38]
Dry ionomer film thickness surrounding the agglomerate	$\delta_M = r_{agg}\left(\sqrt[3]{\frac{(1-\varepsilon_{CL})(1-\varepsilon_{CL}-L_S) + L_{Pt/C}\varepsilon_{CL}(1-\%M)}{L_{Pt/C}}} - 1\right)$	[38]
Liquid water film thickness surrounding the agglomerate	$\delta_w = \sqrt[3]{(r_{agg}+\delta_M)^3 + \frac{s\varepsilon_{CL}(1-\varepsilon_{CL})r_{agg}^3}{L_{Pt/C}}} - (r_{agg}+\delta_M)$	[38]
Concentration of dissolved water	$c_w^d = \rho_M\lambda/EW(1+k_s\lambda)$	[27]
Water content	$\lambda = 0.043 + 17.81\alpha_w - 39.85\alpha_w^2 + 36.0\alpha_w^3$	[35]
Water activity	$\alpha_w = x_w p/p_{sat} + 2s$	[14]
Vapor saturation pressure	$p_{sat} = 9.531\times10^{-4}(T-237)^4 - 3.123\times10^{-2}(T-237)^3 + 3.451(T-237)^2 + 20.96(T-237) + 611.0$	[35-39]
Effective electronic conductivity of catalyst layer	$\sigma_s^{eff} = (L_{Pt/C})^{1.5}\sigma_s$	[37-39]
Effective ionic conductivity of catalyst layer	$\sigma_M^{eff} = (1-\varepsilon_{CL})\left[1 + \frac{(\%M\varepsilon_{CL}-1)}{(1+\delta/r_{agg}+a_0)^3}\right]\sigma_M$	[37-39]
Knudsen diffusivity of species i	$D_{Kn} = \frac{d_{avg}}{3}\sqrt{\frac{8R_gT}{\pi M_i}}$	[36]
Intrinsic diffusivity of species i	$D_{i-g}^0 = \frac{1-x_i}{\sum_{j\neq i}^{n} x_j/D_{i-j}^0}$	[36]

Equivalent diffusivity of species *i*	$D_{i-P}^{0}=\frac{D_{i-g}^{0}D_{Kn}}{D_{i-g}^{0}+D_{Kn}}$	[36]
Diffusivity of oxygen through ionomer film	$D_{O_2-M}=1.3926\times10^{-10}\lambda^{0.708}\exp(\frac{T-273}{106.65})-1.6461\times10^{-10}\lambda^{0.708}+5.2\times10^{-10}$	[38]

673

674

675 Table 5 Mesh characters

676

677

	Channe	GDLs	CLs	Membr	Total elements
Grid 1	10	10	10	10	17500
Grid 2	30	10	10	10	27500
Grid 3	50	10	10	10	37500
Grid 4	50	30	10	10	47500
Grid 5	50	50	10	10	57500
Grid 6	50	50	30	10	67500
Grid 7	50	50	50	10	77500
Grid 8	50	50	50	50	87500
Grid 9	50	50	50	90	97500

678

679

680

681

682

683

684

685

686

687

688

689

690

691

692

693

694

695

696

697

698

699

700

701

702

703 Table 6 Parameters used for model validation and base case condition in the study

704

Symbol	Description (unit)	In house	Wang [41]	Base case
δ_{GDL}	GDL thickness (m)	3.0×10^{-4}	3.0×10^{-4}	3.8×10^{-4}
δ_{CL}	CL thickness (m)	1.5×10^{-5}	1.29×10^{-5}	1.5×10^{-5}
δ_{M}	Membrane thickness (m)	5.5×10^{-5}	1.08×10^{-4}	1.2×10^{-4}
ε_{GDL}	GDL porosity	0.40	0.40	0.40
m_{Pt}	Platinum loading (mg cm^{-2})	0.10 (anode) 0.40	0.40	0.40
f	Platinum mass ratio	20%	40%	40%
L_M	Volume fraction of ionomer	13.3%	32.5%	40%

T	Operating temperature (°C)	80.0	70.0	70.0
p	Operating pressure (atm)	1.0	1.0	1.0
α_c	Cathode transfer coefficient	0.6	2.0	0.7
r_{agg}	Agglomerate radius (m)	1.0×10^{-6}	1.0×10^{-6}	1.0×10^{-6}

Table 7 Terms of thermal sources at various current densities with a single PEMFC

Thermal source (W m^{-3})	0.2 A cm^{-2}		0.6 A cm^{-2}		1.0 A cm^{-2}	
	Anode	Cathode	Anode	Cathode	Anode	Cathode
S_{vd}^T	4.88×10^6 (11.36%)	2.04×10^6 (1.04%)	5.46×10^6 (4.56%)	3.23×10^5 (0.053%	5.54×10^6 (2.84%)	7.93×10^3 (0.00078
S_{dl}^T	2.09×10^3 (0.0049%)	1.80×10^6 (0.92%)	4.55×10^3 (0.0038	2.78×10^7 (4.58%)	1.38×10^3 (0.00071	6.23×10^7 (6.11%)
S_{vl}^T	6.85×10^4 (0.16%)	9.89×10^4 (0.051%	2.08×10^5 (0.17%)	3.03×10^5 (0.050%	3.49×10^5 (0.18%)	5.15×10^5 (0.051%

S_{HOR}^{T}	-3.80×10^{7}	----	-1.14×10^{8}	---	-1.89×10^{8}	---
S_{ORR}^{T}	---	1.91×10^{8} (97.82%	---	5.76×10^{8} (94.88%	---	9.50×10^{8} (93.15%
S_{s}^{T}	3.33×10^{3} (0.0078	3.16×10^{3} (0.0016	3.02×10^{4} (0.025%	2.86×10^{4} (0.0047	8.23×10^{4} (0.042%	7.81×10^{4} (0.0077
$S_{M,i}^{T}$	9.65×10^{3} (0.023%	3.15×10^{5} (0.16%)	8.66×10^{4} (0.072%	2.65×10^{6} (0.44%)	2.34×10^{5} (0.12%)	6.91×10^{6} (0.68%)
Total	4.30×10^{7}	1.95×10^{8}	1.20×10^{8}	6.07×10^{8}	1.95×10^{8}	1.02×10^{9}

Note: total means the sum of the absolute value of each item; the values in brackets are the percentage of each item corresponded to the total heat of the anode and cathode, respectively.

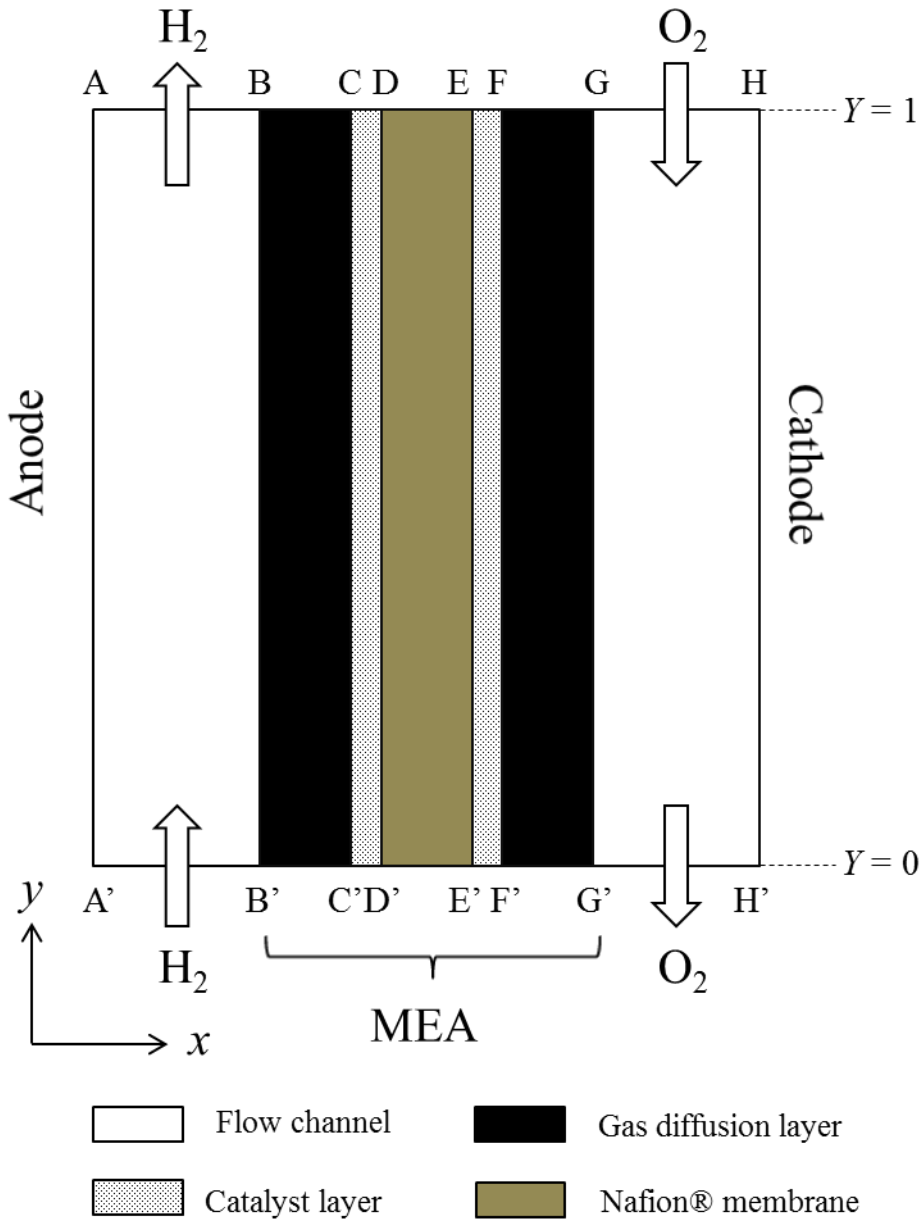

734
735
736

737 Fig. 1 Schematic of PEMFC unit and modelling domain: A-A' - anode flow channel outer boundary; B-B' - anode flow
738 channel-GDL interface; C-C' - anode GDL-CL interface; D-D' – anode CL-membrane interface; E-E' - cathode
739 CL-membrane interface; F-F' - cathode GDL-CL interface; G-G' – cathode flow channel-GDL interface; H-H' – cathode
740 flow channel outer boundary

741
742
743
744
745

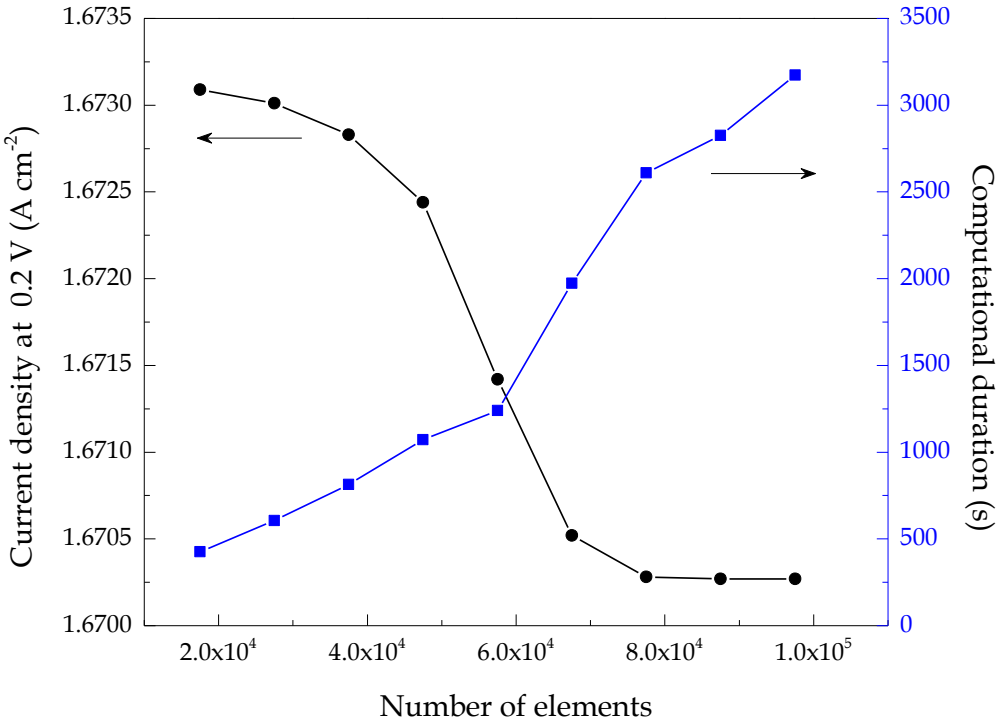

Fig. 2 Effect of mesh characteristics on the current density at 0.2 V

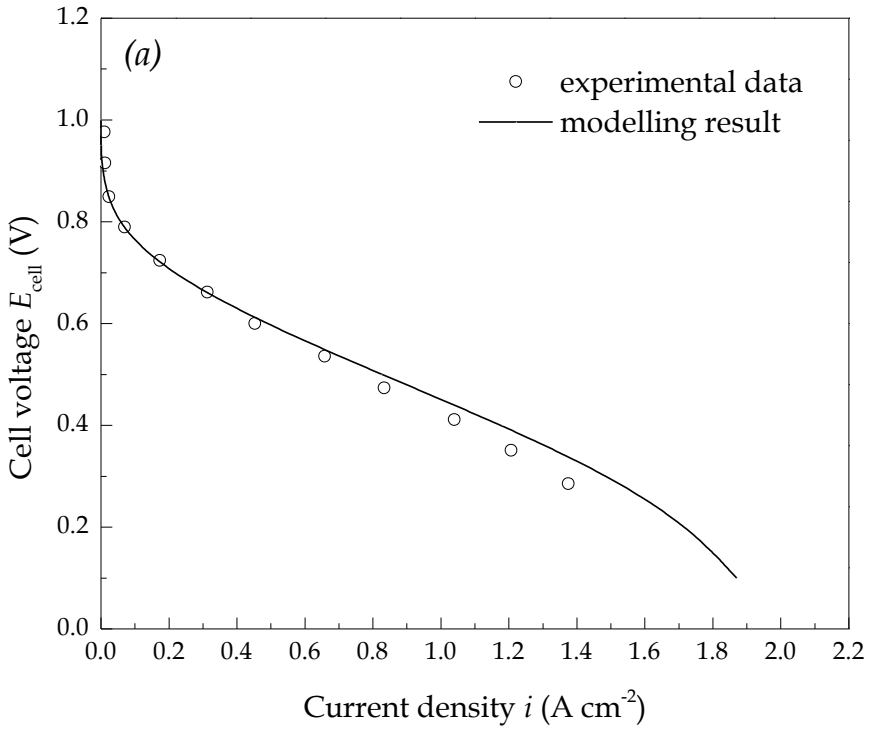
(a)
experimental data
modelling result
Cell voltage E_{cell} (V)
Current density i (A cm^{-2})
0.0
0.2
0.4
0.6
0.8
1.0
1.2
1.4
1.6
1.8
2.0
2.2

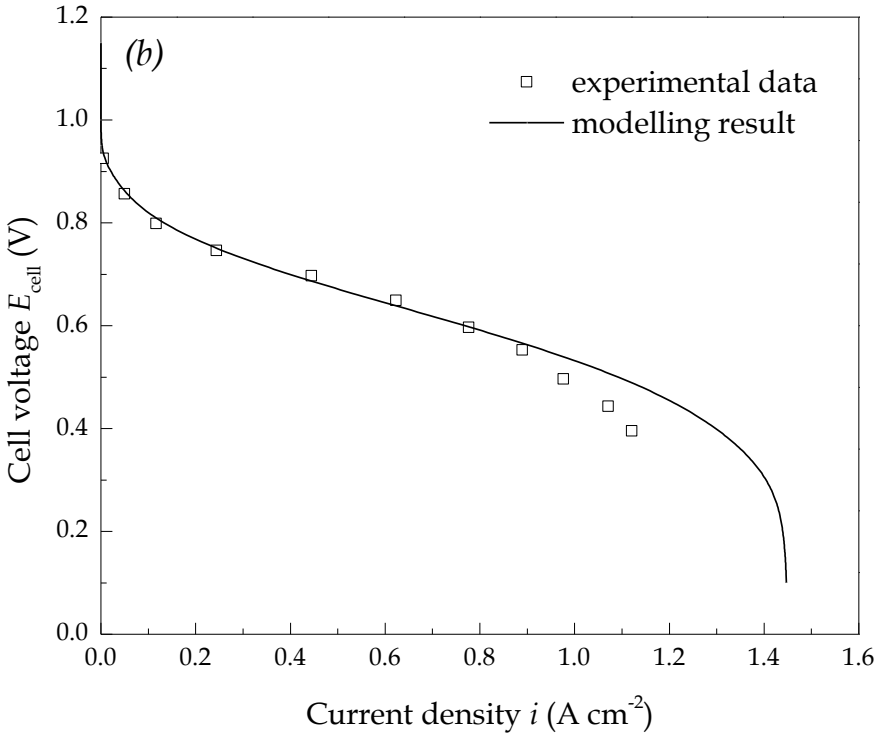

Fig.3 Comparison between the modelling results and experimental data for two cases (a) 80 °C, 20% Pt/C, $m_{Pt,a}$ = 0.1 mg cm^{-2}, $m_{Pt,c}$ = 0.4 mg cm^{-2}, effective area: 1.0 cm × 1.0 cm; (b) 70 °C, 40% Pt/C, $m_{Pt,a}$ = $m_{Pt,c}$ = 0.4 mg cm^{-2}, effective area: 7.2 cm × 7.2 cm

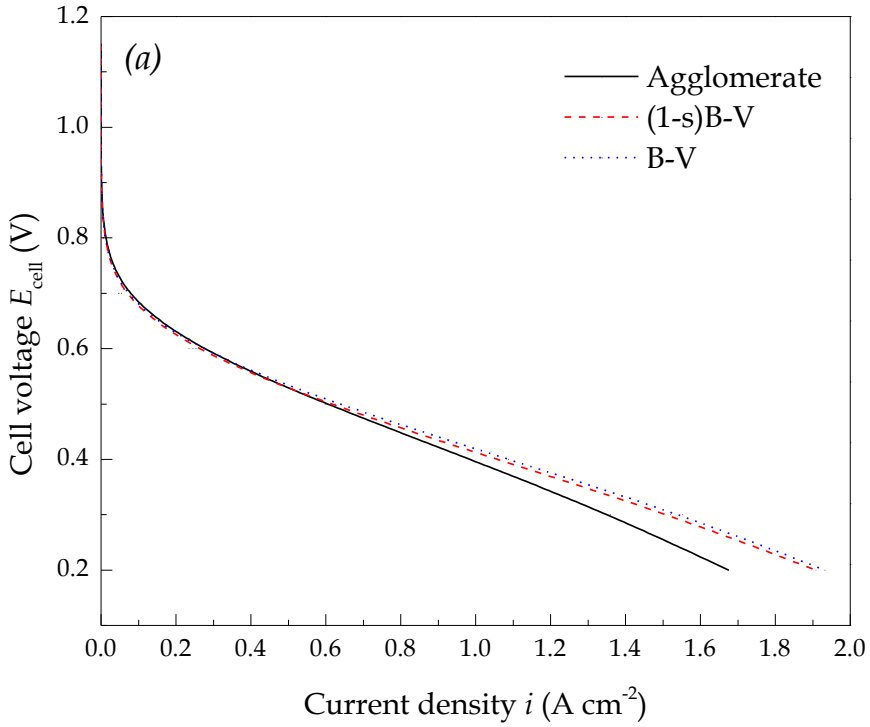

797

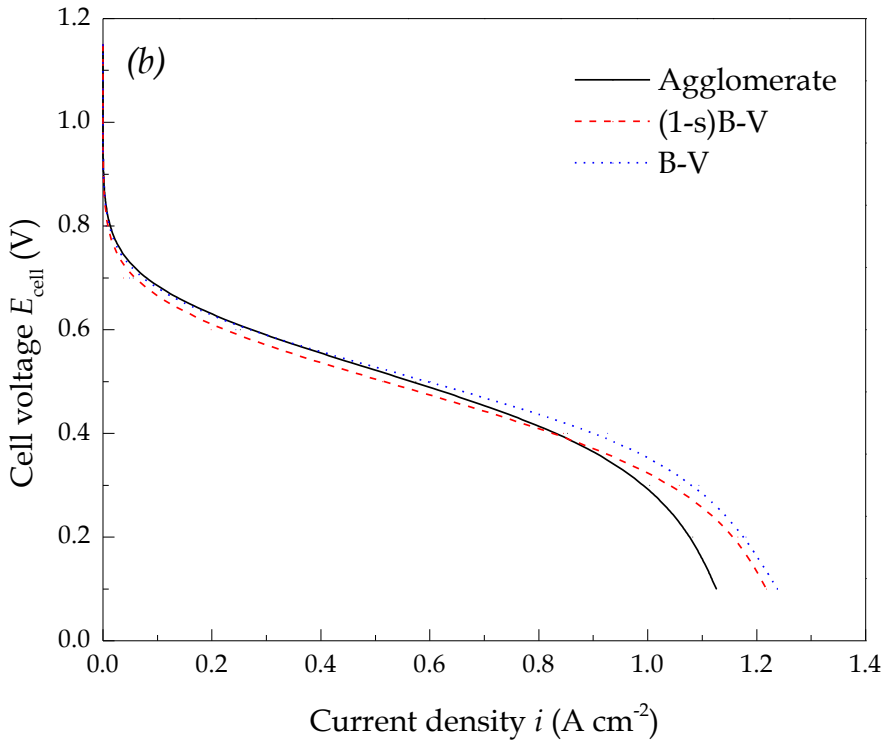

798
799
800 Fig.4 Comparison of three mechanisms for (a) a short 1 cm channel and (b) a long 10 cm channel

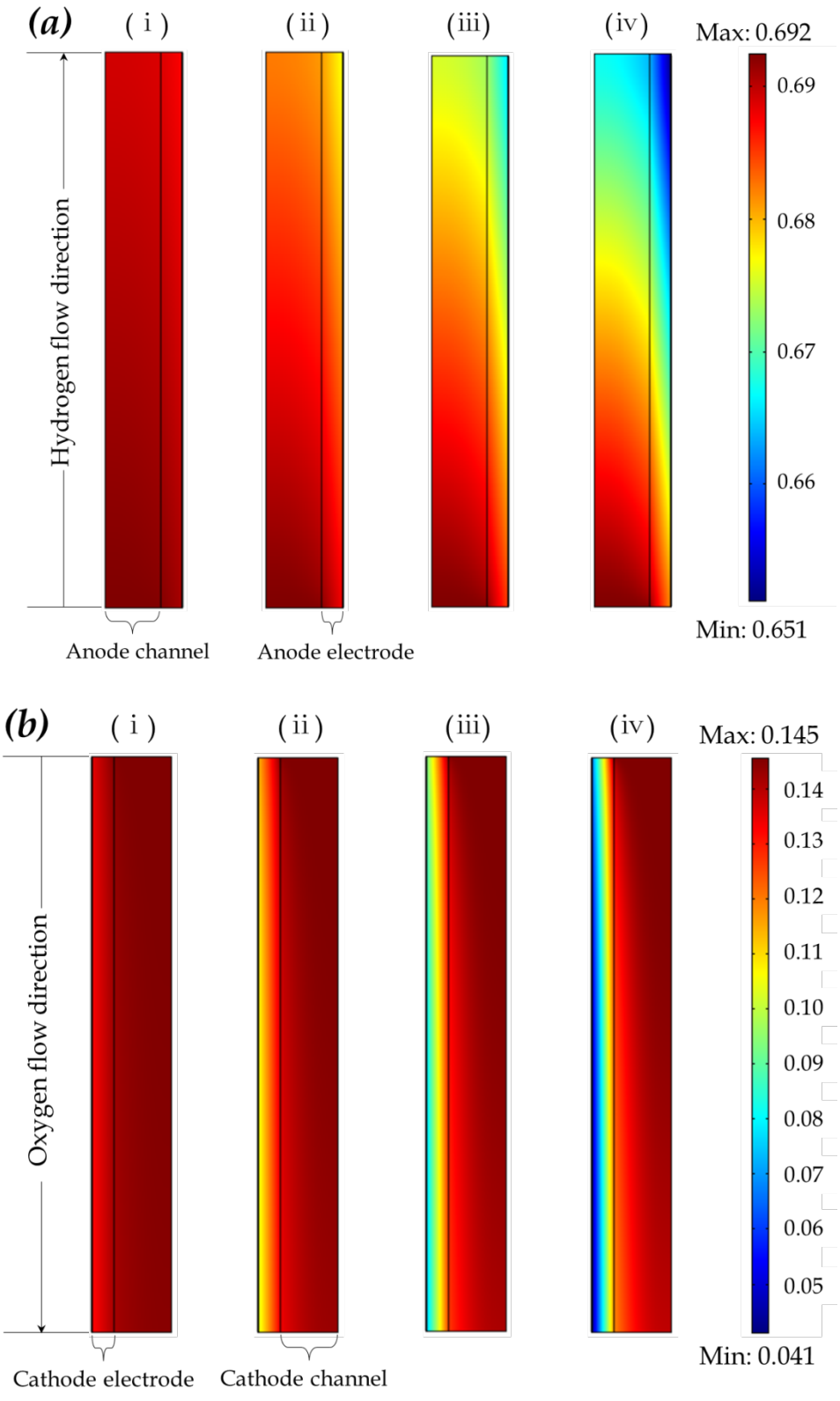

Fig.5 Distribution of mole fractions of (a) hydrogen and (b) oxygen at various current densities at (i) 0.2, (ii) 0.6, (iii) 1.0 and

(iv) 1.4 A cm^{-2}

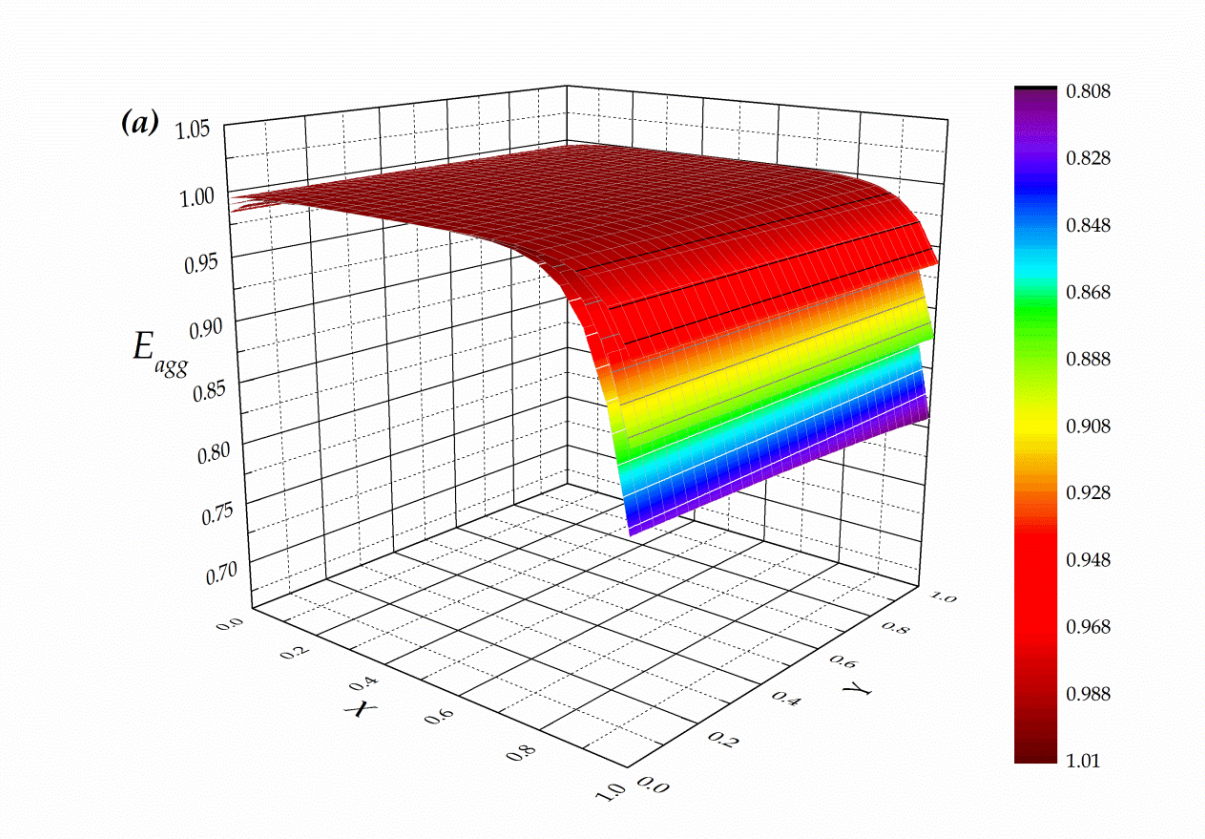
(a)
E_{agg}
1.05
1.00
0.95
0.90
0.85
0.80
0.75
0.70
X
Y
0.0
0.2
0.4
0.6
0.8
1.0
0.808
0.828
0.848
0.868
0.888
0.908
0.928
0.948
0.968
0.988
1.01

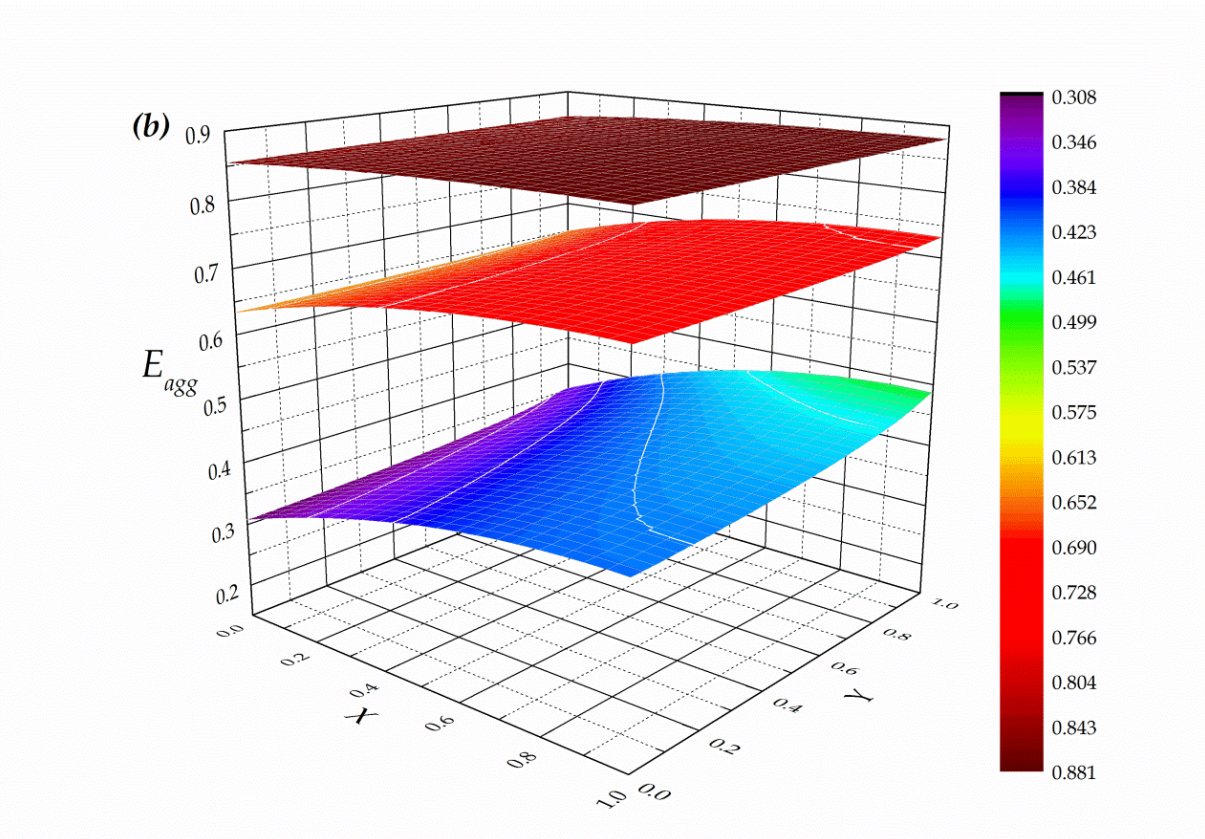
(b)
E_{agg}
0.9
0.8
0.7
0.6
0.5
0.4
0.3
0.2
X
Y
0.0
0.2
0.4
0.6
0.8
1.0
0.308
0.346
0.384
0.423
0.461
0.499
0.537
0.575
0.613
0.652
0.690
0.728
0.766
0.804
0.843
0.881

Fig.6 Effectiveness factor of (a) anode CL and (b) cathode CL at various current densities (from up down: 0.3, 0.7 and 1.2 A cm^{-2})

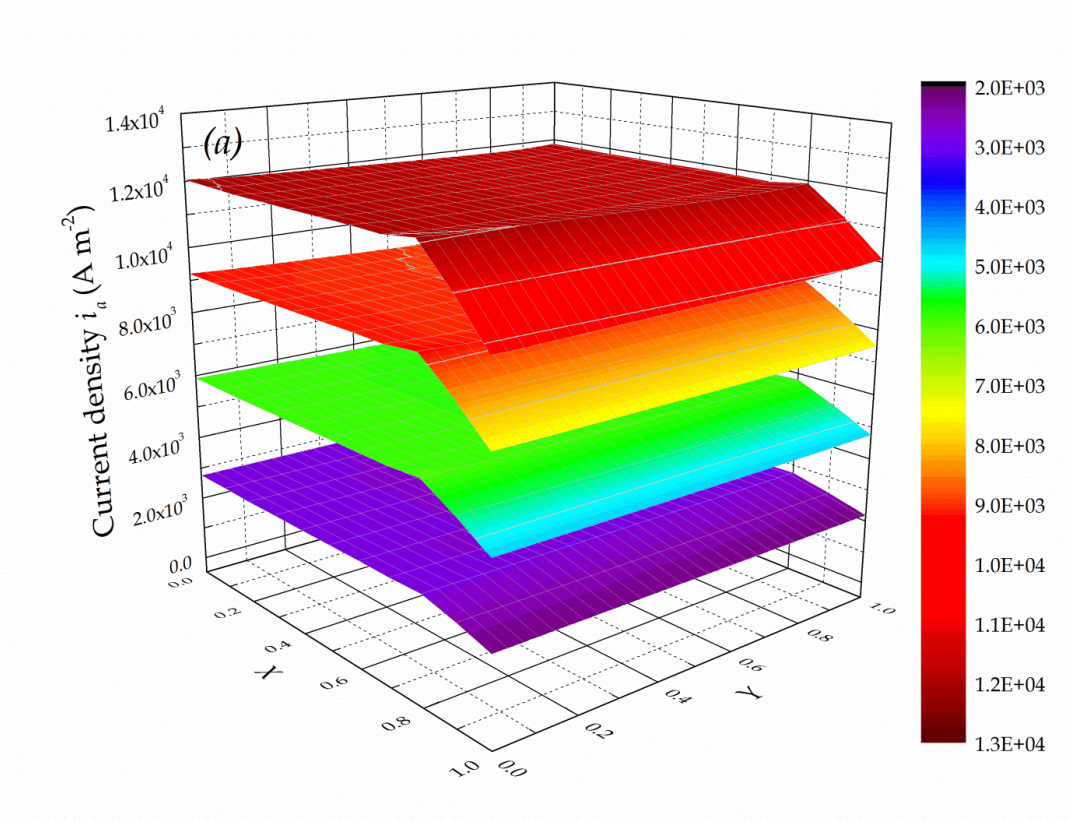

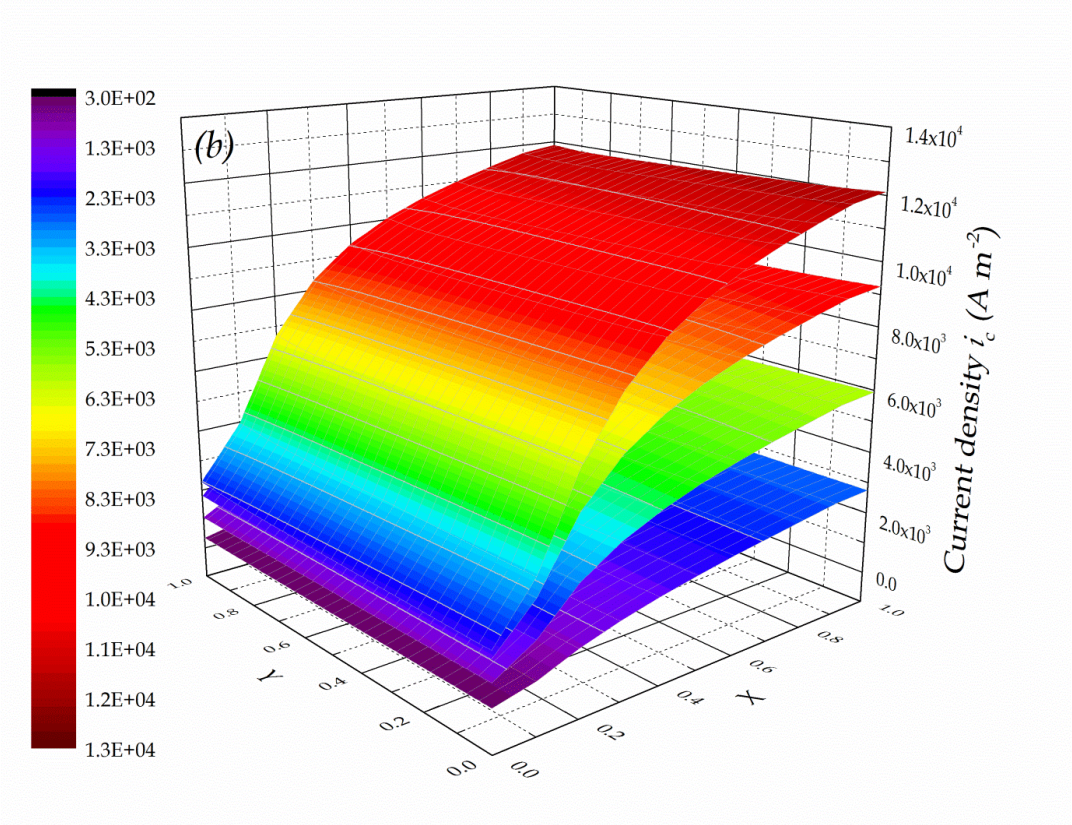

Fig. 7 Current density distribution within (a) the anode CL and (b) the cathode CL (from top down 0.7, 0.6, 0.5 and 0.4 V)

826

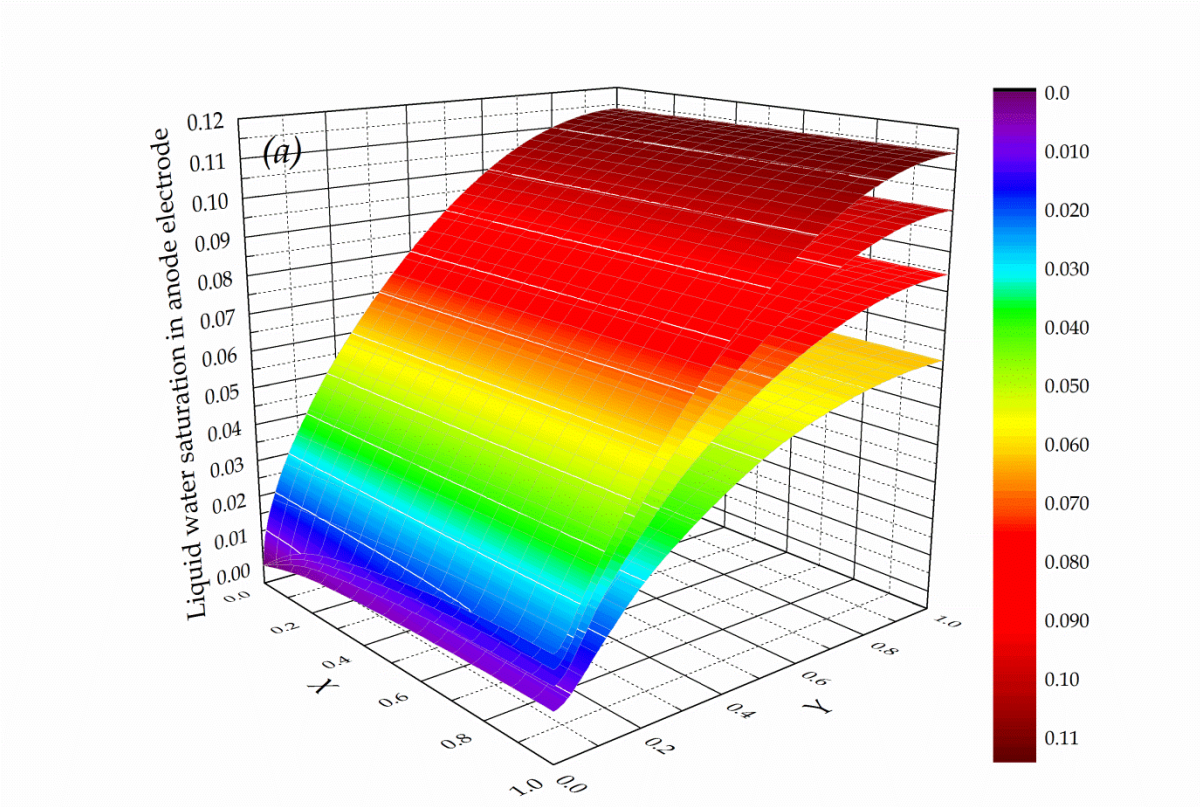

827

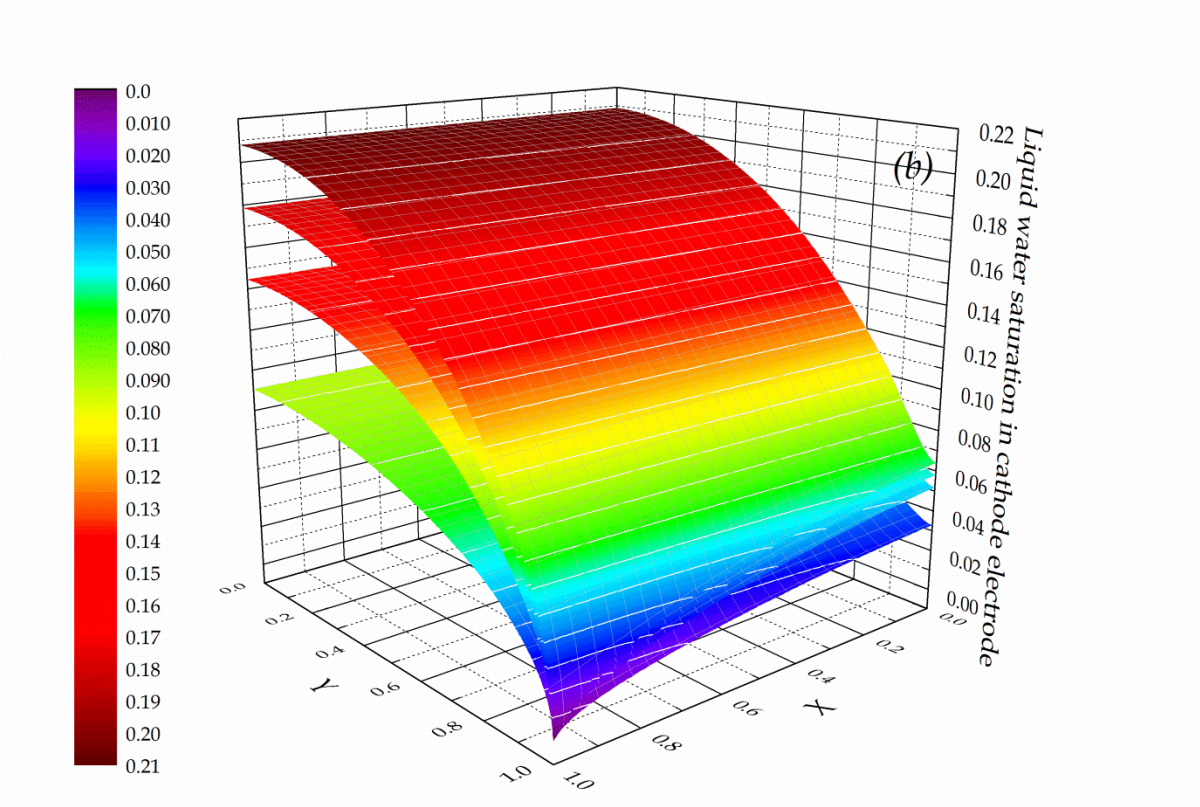

828

829 Fig.8 Liquid water saturation in CLs and GDLs of (a) anode and (b) cathode at various current densities (i = 0.2, 0.6, 1.0 and

1.4 A cm^{-2} from down up)

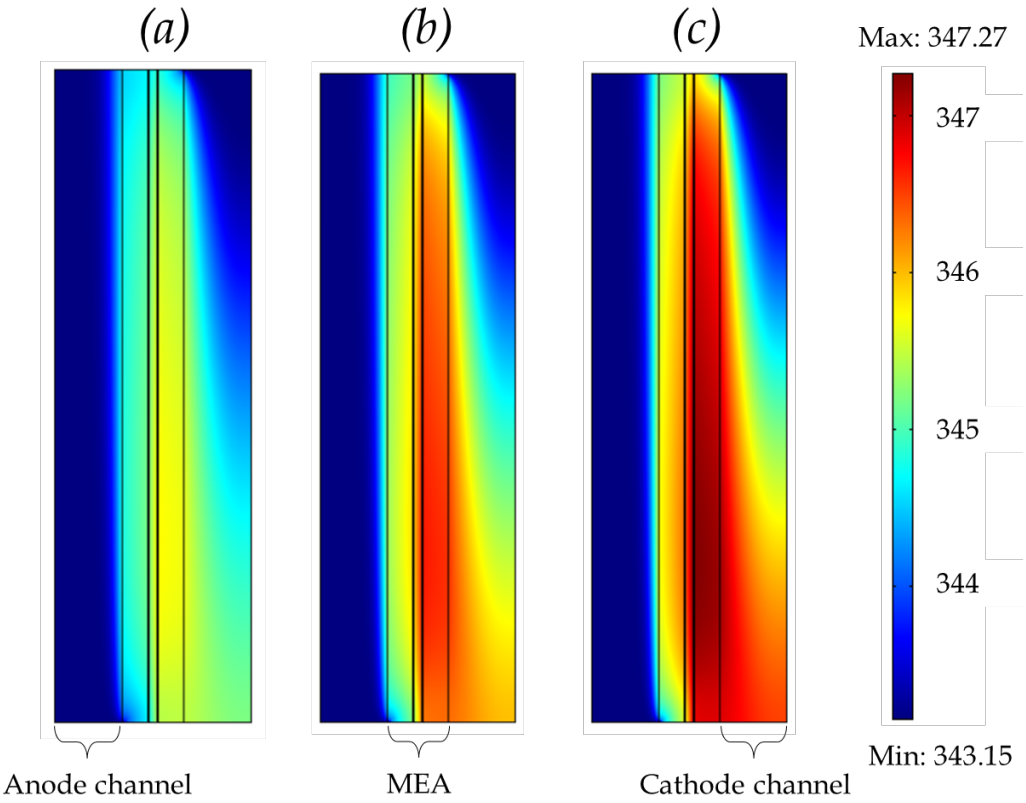

Fig.9 Temperature profiles at various current densities at (a) 0.6, (b) 0.8 and (c) 1.0 A cm^{-2}

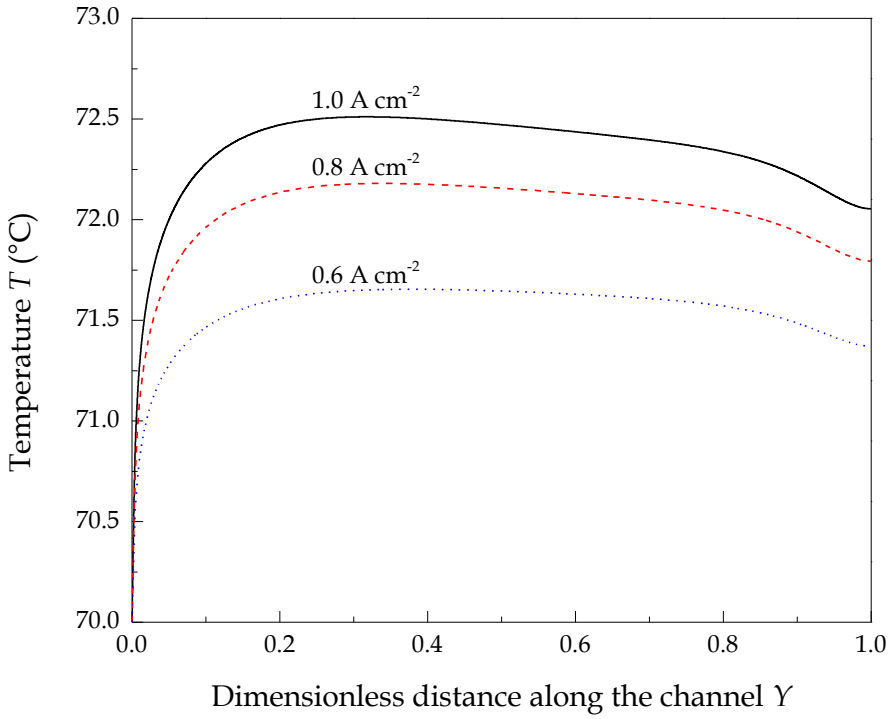

Fig.10 Detailed temperature profiles at anode channel-GDL interface at various current densities at (a) 0.6, (b) 0.8 and (c) 1.0 A cm^{-2}

877
878
879
880
881
882
883
884
885
886
887
888
889
890
891
892
893
894
895
896
897
898
899
900
901
902
903
904

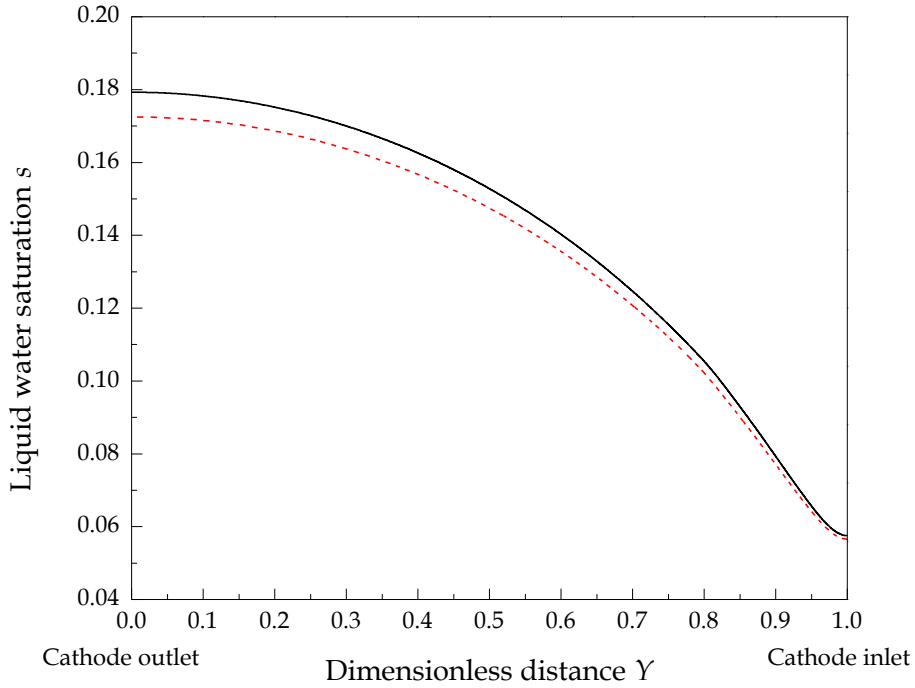

Fig. 11 Comparison of liquid water saturation at the cathode CL-GDL interface at 1.0 A cm^{-2}, predicted by isothermal and non-isothermal models; Solid line - isothermal model prediction, Dash line - non-isothermal model prediction.

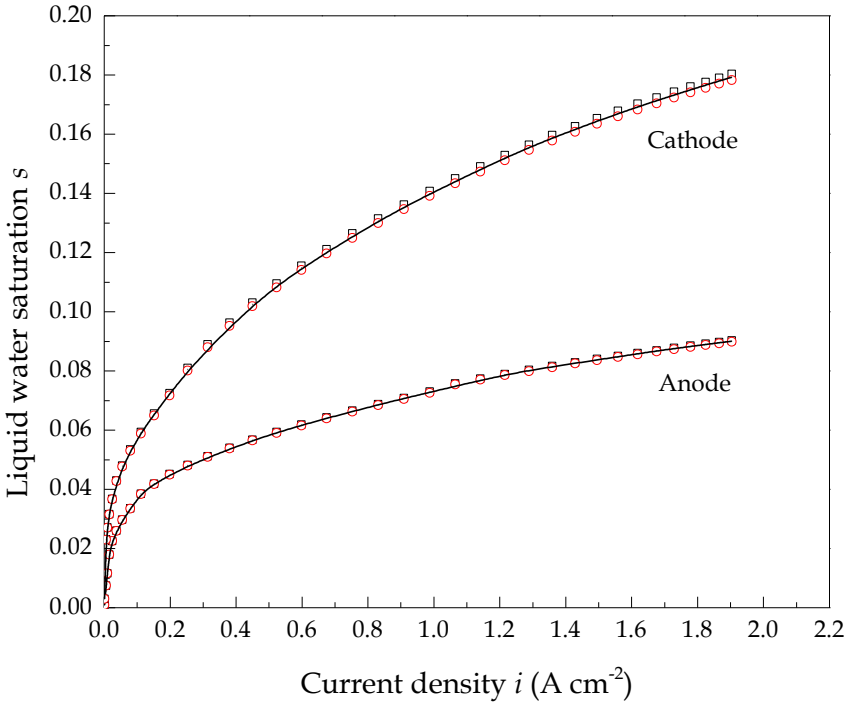

Fig. 12 Average liquid water saturation in both electrodes at various current densities: □- in catalyst layer, ○- in gas diffusion layer, solid line – average value of CLs and GDLs

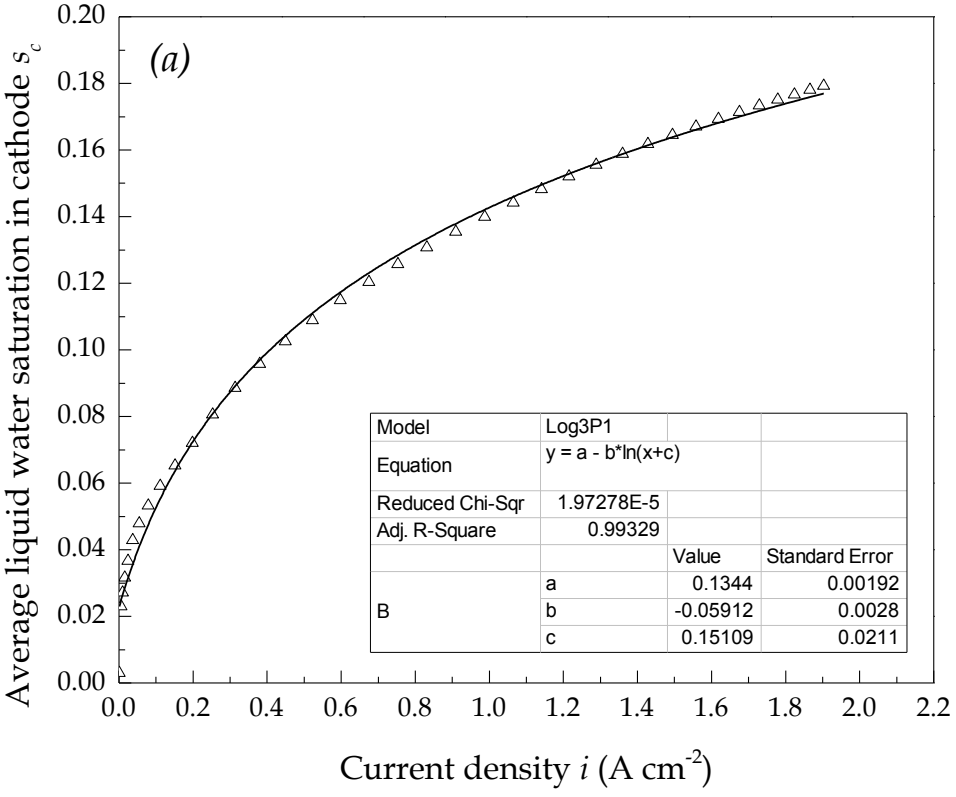
(a)
Average liquid water saturation in cathode s_c
Current density i (A cm^{-2})
0.00
0.02
0.04
0.06
0.08
0.10
0.12
0.14
0.16
0.18
0.20
0.0
0.2
0.4
0.6
0.8
1.0
1.2
1.4
1.6
1.8
2.0
2.2
Model Log3P1
Equation y = a - b*ln(x+c)
Reduced Chi-Sqr 1.97278E-5
Adj. R-Square 0.99329
Value Standard Error
B a 0.1344 0.00192
B b -0.05912 0.0028
B c 0.15109 0.0211

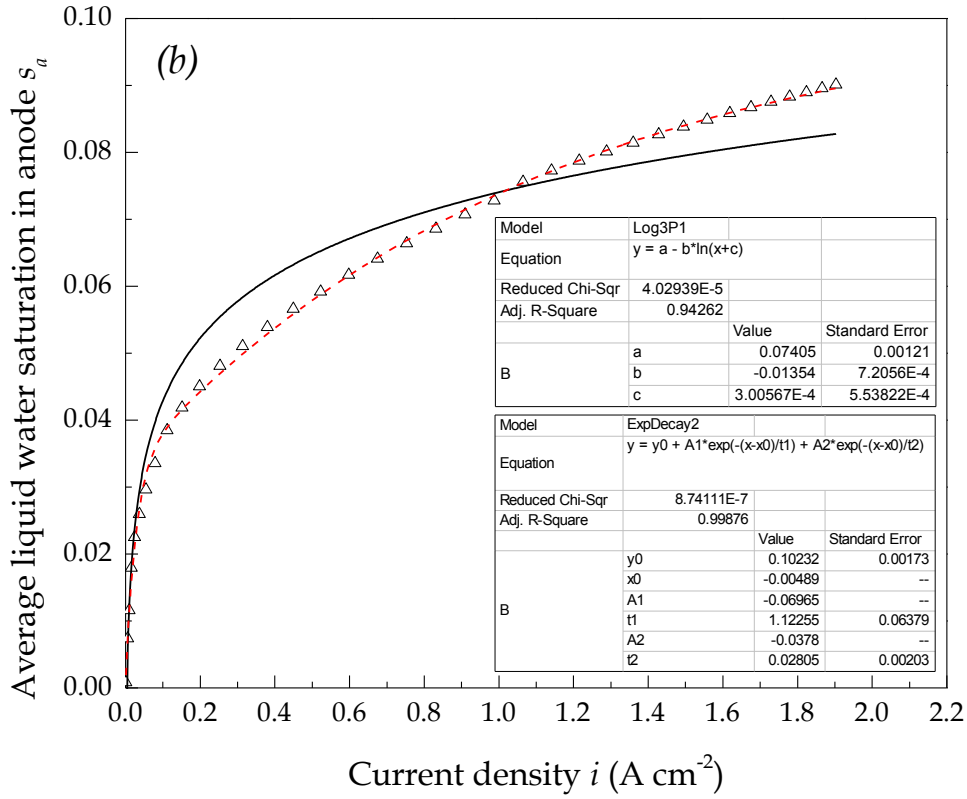

978
979
980

981 Fig. 13 Regression expressions of the liquid water saturation versus current density in (a) cathode (b) anode; ∆-average
982 liquid water saturation, solid line - Log3P1 function fitted, dash line: ExpDecay2 function fitted.

983
984
985
986

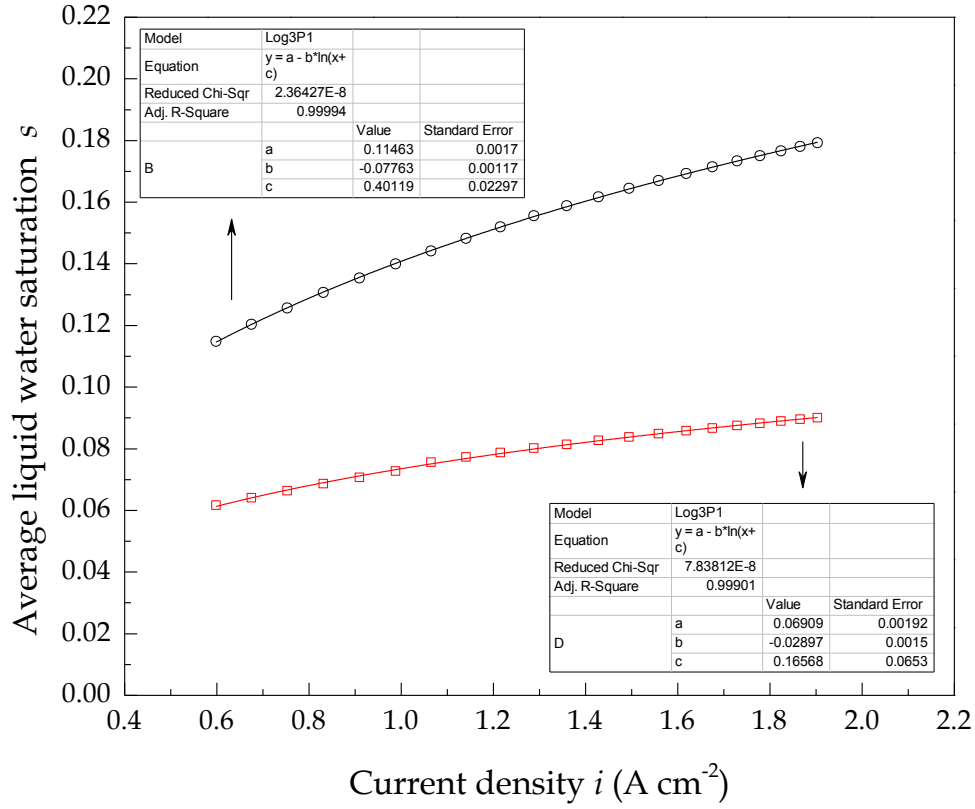

Fig. 14 Regression expressions of the average liquid water saturation in both electrodes versus current density at the current density > 0.6 A cm^{-2}, □- in anode electrode,○- in cathode electrode, solid lines - Log3P1 function fitted

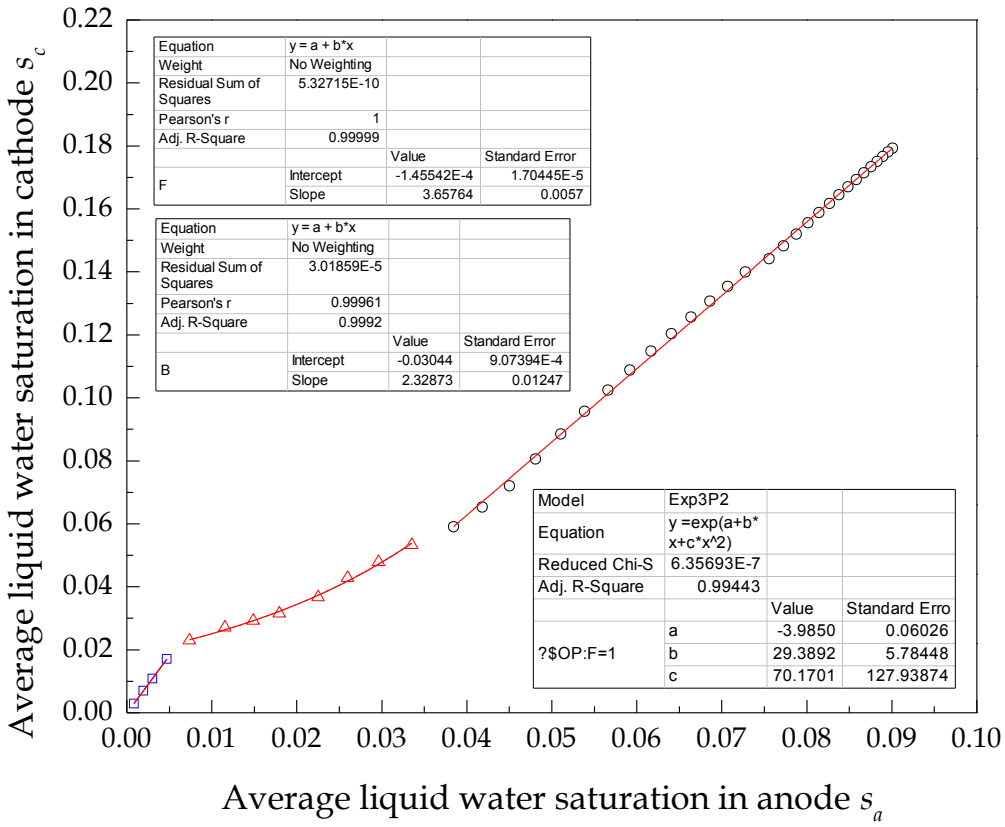

Fig. 15 Relationship between the average liquid water saturation in the anode and the cathode

1034

1035